Article Title: **MC1R reduces scarring and rescues stalled healing in a novel preclinical chronic wound model**

One Sentence Summary: MC1R drives acute and chronic wound repair

AUTHORS:

Holly Rocliffe[1], Shani Austin-Williams[2]*, Georgios Krilis[3]*, Yonlada Nawilaijaroen[1], Antonella Pellicoro[1], Kanheng Zhou[4], Yubo Ji[4], Connor A Bain[5], Yuhang Chen[5], Tianchi Zhou[1], Asok Biswas[6], Michael Crichton[5], Zhihong Huang[4], Andrea Caporali[3], Jenna L Cash[1#]

1. Centre for Inflammation Research, Institute for Regeneration and Repair, 4-5 Little France Drive, University of Edinburgh, Edinburgh, EH16 4UU
2. Biochemical Pharmacology, William Harvey Research Institute, Barts and the London School of Medicine and Dentistry, Charterhouse Square, London, EC1M 6BQ, UK.
3. Centre for Cardiovascular Research, The Queen's Medical Research Institute, 47 Little France Crescent, University of Edinburgh, Edinburgh, EH16 4TJ.
4. School of Science and Engineering, Fulton Building, University of Dundee, Dundee, DD1 4HN, UK
5. Institute of Mechanical, Process and Energy Engineering, School of Engineering and Physical Sciences, Heriot-Watt University, Edinburgh, EH14 4AS, UK
6. Department of Pathology, Western General Hospital, Crewe Road, Edinburgh, EH4 2XU, UK.

* Equally contributed

CORRESPONDING AUTHOR:

Dr Jenna L Cash

Jenna.cash@ed.ac.uk

MC1R reduces scarring and rescues stalled healing in a novel preclinical chronic wound model

Abstract

Cutaneous wound repair typically proceeds uneventfully, resulting in scar formation; however, chronic non-healing wounds (CWs) represent a global and escalating health burden causing substantial morbidity and mortality. Estimated to cost Medicare up to $96.8 billion pa and with a profound paucity of effective therapeutics, novel interventions to rescue the stalled healing response of CWs are urgently needed. In this study, we assess the impact of melanocortin 1 receptor (MC1R) agonism on acute wound healing using a selective agonist, BMS-470539 (MC1R-Ag). MC1R-Ag accelerated wound closure and reepithelialisation in wildtype but not MC1Re/e mice, which harbour a non-functional receptor. MC1R-Ag improved wound perfusion and lymphatic drainage by promoting angiogenesis and lymphangiogenesis, reducing local oxidative stress and inflammation with a knock-on effect of reduced scarring. To assess whether manipulating MC1R would be of benefit in pathological healing, we developed a novel murine model of CWs. By combining advanced age and locally elevated oxidative stress, factors shown to be present in most human CWs regardless of category, resultant wounds expand into the surrounding tissue, generate exudate and slough. Histological comparisons to human CWs demonstrate robust recapitulation of the hallmarks of human disease, including hyperproliferative epidermis and fibrinous exudate. Leveraging this model, we demonstrate that topical administration of MC1R-Ag, following ulcer debridement, rescues the stalled healing response, whereas abrogation of MC1R signalling in MC1Re/e mice exacerbates CWs. Collectively, we highlight MC1R agonism as a candidate therapeutic approach for acute and CWs and remove a critical barrier in CW research by providing a novel preclinical model.

INTRODUCTION

Skin is a fascinating and complex barrier organ comprising multiple layers and cell types that are functionally distinct. Repair of adult cutaneous wounds is typically described in terms of four overlapping, sequential phases: coagulation, inflammation, proliferation/migration and remodelling, culminating in scar formation. Most wounds progress through the phases of healing uneventfully, with the magnitude of the inflammatory response linked to the extent of the resultant scar. However, a growing number of wounds fail to progress through the healing phases in an orderly and timely manner, resulting in a persistent open skin ulcer (1,2). These chronic wounds (CWs), including venous leg ulcers (VLU), diabetic foot ulcers (DFU) and pressure ulcers (PU), become 'stuck' in a chronically inflamed state, unable to heal effectively. CWs represent a global and escalating health burden due to a sharp rise in worldwide incidence of key comorbidities, including diabetes, obesity and advanced age. CW complications include infection, amputation, sepsis and death; hence they impose substantial morbidity and mortality on the individual, healthcare systems and society, with approximately £12 billion pa spent by the NHS on 3.8 million wounds (3–5).

Whilst many other fields have made inspiring leaps in understanding their respective pathologies, resulting in the development of promising therapeutics, research into CWs has long been neglected. Firstly, access to human wound biopsies is not trivial since the necessary infrastructure to obtain these is not readily available to many researchers. Secondly, the lack of a humane animal model that faithfully recapitulates the key features of human CWs has severely hampered CW research. These issues have therefore compromised innovation in new therapies, clinical practices and biomarkers (6–9).

To remove a major barrier for CW research, we have developed an ethical, reproducible, genetically tractable model that reproduces key features of human CWs, including hyperproliferative epidermis, parakeratosis, spongiosis, vasculitis, fibrinous exudate, erythrocyte extravasation, wound expansion and slough generation. We specifically sought to develop a model that is broadly relevant across the ulcer categories of VLU, DFU and PU,

rather than specifically modelling a certain category. Whilst each type of CW is associated with certain comorbidities, for example PU with conditions causing immobility; at their core they share key features. The overwhelming majority of skin ulcers develop in the over 50s, with 95 percent occurring in the over 60s. In addition, VLU, DFU and PU have been shown to exhibit high levels of wound bed oxidative stress. (3,5,10). We therefore used aged animals (18 months) and local elevation of oxidative stress to develop our preclinical model.

This novel model enables the *in vivo* study of candidate therapies to rescue derailed healing responses. Herein, we explore the therapeutic potential of Melanocortin 1 Receptor (MC1R) agonism for treatment of acute and chronic wounds. MC1R is a GPCR expressed peripherally in melanocytes and immune cells, with roles in pigmentation and regulation of anti-oxidative stress mechanisms following UV exposure (11,12). With a functional MC1R, eumelanin, a black pigment, is preferentially produced. A highly polymorphic gene, *MC1R* loss-of-function SNPs result in preferential production of the yellow-orange pigment, phaeomelanin (13). The eumelanin-to-phaeomelanin ratio determines skin and hair colour in humans and coat colour in other mammals. A connection between MC1R and the red-hair phenotype was first established by Valverde et al in 1995, however, since then, variants of MC1R have been linked to an increased risk for skin cancer, UV damage, photoaging and more recently with increased severity of post-burn hypertrophic scarring (12–14). Several studies have explored the role of the receptor in inflammatory responses, including animal models of arthritis. These works have demonstrated that delivery of an MC1R agonist can dampen immune cell recruitment and/or activation and thus inflammation, which in the case of the arthritic joint can prevent cartilage degradation (15,16). To date, no studies have explored the role of MC1R in acute and chronic skin wounds, however, Muffley *et al* have described dynamic spatial localisation of MC1R during cutaneous wound repair, including expression by keratinocytes and immune cells in the acute wound bed (11). Here, we demonstrate that MC1R-Ag promotes acute wound angiogenesis and lymphangiogenesis whilst accelerating wound closure and reducing scarring. We also provide the first description of a

RESULTS

MC1R accelerates wound healing with reduced scarring

To investigate the role of MC1R in wound repair, we used a model of full-thickness excisional skin injury to the dorsal skin of C57Bl/6J wildtype mice. In agreement with Muffley *et al,* we found that *e*xpression of *mc1r* and endogenous ligand precursor *pomc* was induced in acute wounds, peaking at 1 day post-injury (dpi) and declining to healthy skin levels by 7 dpi in both young (8 w old) and aged (18 m old) mice (Fig.1A). To investigate the role of MC1R in cutaneous wound repair we used a MC1R selective agonist, BMS-470539 (MC1R-Ag) as the endogenous agonist αMSH is also a ligand for MC3R and MC5R. MC1R-Ag or vehicle control were administered topically to 4mm full-thickness excisional wounds immediately after injury (Fig. 1A). Macroscopic analysis revealed accelerated wound closure in MC1R-Ag-treated wounds, with maximum differences at 3 and 7 dpi (Vehicle 7dpi, 16.6 ± 3.8%; MC1R-Ag, 7dpi, 4 ± 2.7%, Fig.1B, C). Key repair parameters were assessed, including epithelial tongue length and scab presence as measures of reepithelialisation. An epidermal tongue is the portion of epidermis that has proliferated and migrated under the scab and was found to be significantly longer at 3 dpi with MC1R-Ag-treatment (Vehicle, 270 ± 19 µm; MC1R-Ag, 399 ± 22 µm Fig.1D). Using optical coherence tomography (OCT) imaging of the dynamic changes in epidermal thickness during wound healing, we demonstrate that harnessing MC1R results in earlier proliferation of wound edge epidermis (peak at 3 dpi vs 5 dpi with vehicle-treatment; Fig. 1E), this was followed by a quicker reduction in epidermal thickness by 7 dpi (Vehicle, 140 ± 8 µm; MC1R-Ag, 93 ± 9 µm, Fig. 1E, F). Since re-epithelialisation was completed earlier in MC1R-Ag-treated wounds, this resulted in reduced scab presence at 7 dpi (Vehicle, 71 ± 8.5%; MC1R-Ag, 18 ± 7% of wounds; Fig. 1G,H).

Physiological skin repair culminates in formation of a scar, which predominantly consists of linear bundles of collagen fibers, as opposed to normal dermis, which exhibits a basketweave appearance (1,17). To quantify scarring we measured collagen fiber orientation using a novel

app, FIBRAL (Fig.S1-2). Unwounded skin exhibited abundant collagen with largely randomly-oriented fibers corresponding with a low alignment index (0.152 ± 0.024 ; Fig. 1I-K). In vehicle-treated day 7 wounds, collagen was laid down in a more linear fashion resulting in a high alignment. Wound treatment with MC1R-Ag, however, resulted in collagen deposition with a more random orientation closer to unwounded dermal collagen organisation, which equated to reduced alignment in comparison to vehicle-treated wounds (0.39 ± 0.036 MC1R-Ag vs 0.58 ± 0.045 vehicle; Fig. 1I-K). We also assessed collagen quantity in Picrosirius Red-stained wound sections, finding that treatment with MC1R-Ag accelerated the rate of collagen deposition (66.9 ± 1.85% MC1R-Ag vs 56.5.2 ± 3.64% vehicle vs unwounded 74.5 ± 6.17%). Thus a downstream consequence of wound MC1R-Ag treatment is reduced scarring through improved collagen deposition quality and quantity to levels approaching unwounded skin.

MC1R modulates the wound environment during healing

Wound repair from the late stages of fetal development onwards is accompanied by robust recruitment of innate immune cells to the wound. The optimal balance between sufficient leukocyte recruitment to combat any invading microorganisms versus excessive pathological inflammation, which contributes to scarring, is of critical importance in any tissue repair response or therapeutic treatment (1). We monitored leukocyte recruitment dynamics during dermal wound repair, finding that MC1R-Ag administration inhibits neutrophil recruitment to excisional cutaneous wounds (Fig. 2A). Surprisingly, MC1R-Ag increased F4/80$^+$ MΦ recruitment to day 7 wounds (Fig. 2B), however we noted that MΦ distribution in the skin adjacent to the wound was limited by MC1R-Ag treatment, unlike vehicle-treated day 7 wounds where an F4/80$^+$ infiltrate is present in the wound adjacent dermis (Fig. 2C-D). We noted no clear change in wound MΦ morphology, however, a marked improvement in erythrocyte clearance (Prussian blue$^+$ cells; Fig. 2E) was observed, along with significantly reduced wound TNFα (Fig. 2F) and oxidative stress (dihydrorhodamine$^+$ cells; Fig. 2G).

Collectively, these data suggest that MC1R agonism modulates the wound microenvironment, possibly resulting in a shift towards the repair phase (proliferation/migration and remodelling).

Harnessing MC1R drives angiogenesis and lymphangiogenesis at sites of cutaneous repair

Angiogenesis and lymphangiogenesis are processes that principally occur either during early development or during wound repair or inflammation (18). Wound angiogenesis is required to enable delivery of oxygen and nutrients to the metabolically demanding repairing tissue, with impaired angiogenesis observed in aberrant healing scenarios including DFUs (5,19). Lymphatic vessels are thought to be important in wound healing as they drain interstitial fluid to reduce tissue swelling and permit the transportation of immune cells to lymph nodes (20). We therefore investigated the effect of MC1R-Ag on angiogenic and lymphangiogenic responses during cutaneous wound repair (Fig. 3). As we and others have previously shown (21–23), the time course of angiogenesis preceded that of lymphangiogenesis with angiogenic sprouting occurring as early as 3 dpi, peaking at 7 dpi and vascular remodelling, including trimming of superfluous vessels occurring thereafter (Fig. 3A,D; Fig. S3). The lymphangiogenic response, however, was evident at 7 dpi, and appeared to still be ongoing at our latest time point 14 dpi (Fig. 3A). Wound treatment with MC1R-Ag profoundly enhances the angiogenic (155%) and lymphangiogenic (216%) responses with increased vessel density over vehicle-treated wounds (Fig. 3A-B). Vessel width analysis reveals that MC1R-Ag administration results in increased lymphatic vessel width but equivalent blood vessel widths in comparison to vehicle control (Fig. 3C). OCT angiography was performed to verify if the $CD31^+$ cell areas detected via immunofluorescence staining were functional, perfused blood vessels. Indeed, notable wound bed perfusion is detectable 7 dpi with MC1R-treatment and declines thereafter (Fig. 3D). To determine whether MC1R-Ag was improving wound vascularisation via direct MC1R-mediated effects on endothelial cells, we employed a microvascular endothelial cell tube formation assay. MC1R-Ag significantly increased

readouts of *in vitro* angiogenesis, including total mesh area, branching interval and total segment area (Fig. 3E-G, Fig. S4). MC1R knockdown using siRNA demonstrated that these angiogenic effects of BMS-470539 are mediated by MC1R (Fig. 3F, Fig.S5). To assess wound lymphatic vasculature function, we employed a lymphatic drainage assay, whereby Evans Blue dye injected into wounds was quantified in skin-draining lymph nodes. We confirm that the observed increase in lymphatic vessel area translated to improved lymphatic drainage (Fig. 3H). Collectively, we demonstrate that BMS-470539 acts via endothelial cell MC1R to drive angiogenesis and lymphangiogenesis, resulting in improved wound bed blood supply and lymphatic drainage.

Lack of functional MC1R impairs acute wound healing

In humans and mice, lack of a functional MC1R due to spontaneous mutation, results in preferential production of the yellow-orange pigment, phaeomelanin in the skin and hair. To establish the impact of MC1R on wound healing, we generated 4 mm wounds in MC1Re/e mice, which harbour a non-functional receptor (ginger hair; C57Bl/6J background) and in wildtype (black hair; C57Bl/6J) mice. We discover that lack of functional MC1R profoundly impairs healing, with significantly delayed wound closure detectable at 1, 7, 10 and 14 dpi (7 dpi – MC1Re/e, 27.4 ± 2.1%; C57B/6J, 7.36 ± 0.83% of initial wound area; Fig. 4A-D). Scab loss, an indicator of complete reepithelialisation, is also delayed with 95% of MC1Re/e wounds retaining a scab at 7 dpi in comparison to 68.8% of wildtype control wounds (MC1Re/e + vehicle, 95 ± 5.1%; MC1Re/e + BMS-470539, 90.2 ± 6.1%; C57Bl/6J, 68.8 ± 7.84; Fig. 4E). MC1R agonist, BMS-470539, is unable to impact the wound healing response in MC1Re/e mice.

We have established that harnessing MC1R using a selective agonist, BMS-470539, drives wound bed vascularisation and promotes acute wound repair with reduced scarring. However,

acute wounds typically heal without complications, therefore we asked whether MC1R agonism would be of benefit in the context of non-healing wounds.

Development of a preclinical chronic wound model

CWs represent a major unmet need and exhibit profoundly impaired wound vascularisation, which is thought to be an important determinant of wound outcome. We reasoned that administration of MC1R-Ag in a preclinical CW model would allow us to determine whether harnessing this pathway holds merit as a novel intervention for pathological healing. To get to this point, we first needed to develop a humane model that reproduces the hallmarks of human CWs, both on a macroscopic level (eg. exudate, slough, wound expansion) and a microscopic level (eg. hyperproliferative epidermis, extravasated erythrocytes, fibrinous exudate, parakeratosis). We specifically sought to develop a model that is broadly relevant across the ulcer categories of VLU, DFU and PU, rather than specifically modelling a certain category. Whilst each type of CW is associated with certain comorbidities, for example PU with conditions causing immobility; at their core they share key features. The overwhelming majority of skin ulcers develop in the over 50s, with 95 percent occurring in the over 60s. In addition, VLU, DFU and PU have been shown to exhibit high levels of wound bed oxidative stress (3,5,10). Taking inspiration from the advantages and limitations of current murine models (6,7,24,25), we developed our unique model using aged animals and local elevation of oxidative stress (Fig. 5A).

A 4 mm excisional wound was made to the dorsal skin of aged mice, topical Glutathione peroxidase (GPx) inhibitor, mercaptosuccinic acid (MSA) was applied, following by a transparent Tegaderm dressing (Fig. 5A). The wounds expanded into the surrounding tissue 5-fold over the first 7 dpi with the tissue taking on a macerated (white) appearance (approx. 1 dpi), followed by a thin red border appearing around the macerated area at 3 dpi but absent by 7 dpi. The wounds produced exudate and slough, stabilised at this size for the duration of the experiment (Fig.5A-B) and were well tolerated by the animals (Fig. S6). Wound architecture was compared between the well established acute excisional wound model (Fig. 5C-D), the new CW model (Fig. 5G-H) and a cohort of 44 human CWs (28 VLU, 9 DFU, 7 PU;

Fig. 5E-F, Fig. S7). During successful skin repair, at only 1 dpi a scab has formed as a result of haemostasis, reepithelialisation is not evident, provisional matrix has been deposited and a rich PMN infiltrate is notable (Fig. 5C). In contrast, at 14 dpi, reepithelialisation is complete, scab loss has occurred, few PMN remain and the wound bed is well vascularised (Fig. 5D).

In human CWs we find that fibrinous exudate, hyperproliferative epidermis, PMN infiltrate and vasculitis are consistently present, being identified in 86-100% of DFU, VLU and PU. Hypogranulosis (78-100%), extravasated erythrocytes (71-100%), parakeratosis (57-78%) and spongiosis (67-100%) were also common histomorphological features (Fig. 5E-F, Fig. S8). Hemosiderin deposition proved to be the most variable feature, found in all VLU, 56% of DFU but none observable in PU. This likely relates to specific co-morbidities including venous stasis that are most commonly found in patients with VLUs (Fig. 5E,F, Fig. S7-8). In our preclinical CW model, macroscopic and histomorphological analysis revealed excellent recapitulation of hallmarks of human CWs (Fig. 5G,H). Notable, were a severe lack of granulation tissue formation, substantial and persistent fibrinous exudate, presence of extravasated erythrocytes and subcutaneous fat necrosis. Major disturbance to epidermal physiology was evident through hyperproliferation, spongiosis and parakeratosis, along with a complete failure of wound reepithelialisation. Whilst exudate and slough were abundant, scab formation was absent (Fig. 5G,H).

MC1R agonist rescues the stalled healing response in a preclinical chronic wound model

In the clinic, non-healing wounds are typically managed in the community, with dressing changes and basic wound debridement performed as part of standard wound care (26). Effective wound debridement is thought to partially stimulate healing, but in complex wounds, is typically insufficient to result in complete repair. To assess a potential therapeutic intervention, we therefore debrided the wounds 7 dpi (Fig. 6A,B). Topical vehicle-control and

MC1R-Ag were administered in a pluronic hydrogel immediately after debridement and at each subsequent dressing change 3 and 5 days later (Fig. 6A,B). Vehicle-treated debrided wounds mimicked the hallmarks of human CWs (Fig. 6B,C), including extravasated erythrocytes, PMN infiltrate, fibrinous exudate, spongiosis, parakeratosis, a lack of wound vascularisation and absence of reepithelialisation (Fig. 6B,C), whilst exhibiting a partial stimulation to healing, evident as a 30% reduction in wound area at 14 dpi. However, MC1R-Ag treatment following debridement rescued the healing response, with an additional 33% reduction in wound area over debridement alone. Here, we observed partial reepithelialisation, as evidenced by formation of epithelial tongues, minimal fibrinous exudate was present and a vascularised granulation tissue formed (Fig. 6B,D). In contrast, MC1Re/e CWs produced copious wound exudate both pre and post-wound debridement (Fig. 6E,H) such that 88% exhibited notable exudate 14 dpi in comparison to 56% of vehicle-treated wildtype wounds. Presence of wound exudate was reduced with MC1R-agonist treatment with only 20% of wounds displaying visible exudate (Fig. 6F,H). Importantly, NETosis, spongiosis and hemosiderin deposition were notable features of MC1Re/e CWs, but extravasated erythrocytes were not observed (Fig. 6I).

DISCUSSION

In this study, we assessed the impact of harnessing MC1R on acute wound healing using a selective agonist, BMS-470539. MC1R agonism resulted in accelerated wound closure and reepithelialisation in wildtype but not MC1Re/e mice which harbour a non-functional receptor. MC1R-Ag improved wound perfusion and lymphatic drainage by promoting angiogenesis and lymphangiogenesis, reducing local oxidative stress and inflammation with a knock-on effect of reduced scarring. Our data suggest that MC1R enables wounds to transition to the proliferative phase quicker to effect efficient healing. Surprisingly we noted minimal effects on leukocyte recruitment, however, it is entirely possible that some of the impact on wound healing may be through modulating leukocyte phenotype or via leukocyte lineages out with the scope of this

study. Nevertheless, MC1R-Ag acts directly on endothelial cells to drive microvascular endothelial cell sprouting and mesh formation and may therefore hold promise for pathologies characterised by poor vascularisation.

MC1R activation also has potential anti-fibrotic properties. Collagen alignment plays a significant role in scar quality, with a disordered collagen architecture being characteristic of an unwounded dermis. Using simulations and multi-scale mathematical modelling, McDougall *et al* derived equations to elucidate the molecular cause of alignment during collagen deposition. Their results suggest that a localised chemoattractant gradient, with greater effects on only those fibroblasts in the vicinity of the wound, produces a collagen pattern that is highly disordered (27). This could be the driver behind reduced collagen alignment in MC1R agonist-treated wounds; macrophages were more restricted to the wound site and could thus provide localised chemoattractants. The inflammatory profile at the wound site and in the neighbouring unwounded dermis could be more comprehensively analysed for mediators known to modulate fibroblasts biology, to further elucidate the mechanism of the observed effect of MC1R-Ag on scarring.

Given that the majority of acute wounds heal without complication, and CWs represent a profound and escalating burden to individuals and healthcare systems (3), we sought to develop a preclinical CW model to act as a platform for testing of novel interventions such as MC1R-Ag. Equally importantly, the provision of such a model has long been recognised as essential to better understand the disease process without the risk of clinical harm (7). Here, we utilised the mouse as our model organism, since they are amenable to genetic manipulation, reproduce rapidly and are easy to house and maintain.

As described by Frykberg and Banks, CWs have variable underlying pathologies, including diabetes, immobility, venous stasis and can be divided into categories based on these, such as DFU, PU and VLU. However, almost all CWs occur in the over 50s and exhibit elevated

oxidative stress (5). Whilst CWs also typically exhibit pathological alterations in the balance of various MMPs and TIMPs, manipulation of these pathways is not trivial (28). We therefore developed our model by combining advanced age and locally elevated oxidative stress, which proved to accurately mimic many of the hallmarks of human CWs. The model can now be used to study CW development and persistence with the view of identifying novel tractable targets for therapeutic gain.

Inevitably, every preclinical model has limitations and it is important to be aware of these, particularly when translating findings to the clinic. With respect to the preclinical CW model we have described here, the key considerations are concerning the unavoidable differences in skin anatomy between mouse and human (29). In human, the epidermis and dermis are thicker and the skin is firmly adherent to the fascia, whereas in mouse, the skin is typically not adherent to the underlying fascia. We note that in our model and the context of chronic inflammation, the wounds can adhere to the fascia. Indeed, others have noted a major contribution of fascia-derived fibroblasts to murine acute wound scarring, though in this scenario the wound is only temporarily adherent to fascia (30). Here, we deliberately avoided generating a diabetic chronic wound model, conscious of the need for a model broadly applicable to all categories of human CWs and to the limitations of murine diabetes models, which are typically monogenic and include leptin abnormalities, unlike human type 2 diabetes, which is polygenic, multifactorial and absent in leptin aberrations. In addition, the duration of human CWs has always posed a challenge with respect to preclinical model development. It is simply not ethical nor feasible, due to the short lifespan of mice, to model CWs that persist for many years as they can in human. Instead, we model the development and shorter-term persistence of CWs in our murine model, consciously choosing time points that provide a comparison to the well-published acute wound model. In doing so, we provide the opportunity We are however encouraged by our histomorphological analysis, which revealed many of the same features of human CW epidermis, including clear epithelial hyperproliferation, failure to reepithelialise and parakeratosis.

The cellular and molecular mechanisms behind skin repair and scar formation and particularly development and persistence of CWs have yet to be fully elucidated, this study suggests that targeting MC1R may represent an effective strategy to rescue failed healing and reduce acute wound scarring, potentially by enabling wounds to transition to the proliferative phase quicker. We anticipate that our novel model will become a valuable tool to interrogate ulcer formation and persistence along with testing of novel interventions, whilst the discovery of MC1R agonists role in angiogenesis and lymphangiogenesis opens promising new avenues for the therapeutic exploitation of this pathway for wound healing.

MATERIALS AND METHODS

BMS-470539

MC1R agonist, BMS-470539, was synthesised by Mimotopes (Minneapolis, USA), reconstituted (1 mM in PBS + 0.1% BSA) and stored at -80°C for up to 6 months. BMS-470539 was diluted from fresh aliquots for each experiment.

Animals

All experiments were conducted with approval from the University of Edinburgh Local Ethical Review Committee and in accordance with the UK Home Office regulations (Guidance on the Operation of Animals, Scientific Procedures Act, 1986) under PPL PD3147DAB. C57Bl/6JCrl and MC1Re/e mice on a C57Bl/6JCrl background were bred in-house (LFR at BioQuarter site), maintained in conventional cages on a 12:12 light:dark cycle with *ad libitum* access to standard chow and water under a SPF environment. Animals were housed 3-5 per cage in a temperature (22-24C) and humidity controlled room. All animals were housed in the same room throughout their lifespan. Environmental enrichment was provided in the form of dome homes, a tunnel and wooden chew sticks. Health checks were performed on all animals prior to wounding, including baseline weight measurements, malocclusion and skin injuries due to

fighting. Animals with malocclusion were excluded from the study and those with small skin injuries due to historic fighting were included providing wounds could be made without involvement of the previous injury area. Only healthy animals that were not involved in previous procedures were used for experiments. The chronic wound model described below was developed following the 3Rs framework (31) and with regular input from the NVS (Named Veterinary Surgeon, Nacho Vinuela-Fernandez).

Aging mouse colony

Once animals reached 12 months of age, several parameters of health were monitored on a weekly basis to determine animal welfare. Parameters were weight (as compared to baseline 12 mo weight), body condition scores (as determined by visual and physical examination of each animal in accordance with the University of Edinburgh Veterinary Scientific Service guidelines) and behaviour. Weight loss of 10% and/or an increase in body condition score or evident lack of expected behaviour (interaction, movement) resulted in the animal being assessed by a vet.

Acute skin wounds

Male and female mice (7-9 weeks old) were randomly assigned a treatment group and anaesthetized with isoflurane (Zoetis, Leatherhead, UK) by inhalation. Buprenorphine analgesia (0.05 mg/kg, s.c, Vetergesic, Amsterdam) was provided immediately prior to wounding and dorsal hair was removed using a Wahl trimmer. Four full-thickness excisional wounds were made to the shaved dorsal skin using sterile, single use 4 mm punch biopsy tools (Selles Medical, Hull, UK). Wounds were photographed with a Sony DSC-WX350 and a ruler immediately after wounding and also on days 1, 3, 7, 10 and 14 post-wounding. Vehicle (PBS) or BMS-470539 were delivered topically by pipette into the wound cavity immediately after wounding (40 μl in a 30% Pluronic F-127 gel (liquid at 4ºC, but solidifies at room temperature; Sigma Aldrich). Wound areas were calculated using ImageJ software.

Mice were housed with their previous cage mates in a 28C warm box (Scanbur, Denmark) overnight following wounding, with paper towels used as bedding to avoid sawdust entering the open wounds. Dome home entrances were enlarged to prevent animals scraping their dorsal skin wounds. Animals were moved into clean conventional cages at 22-24C the following morning.

Chronic skin wounds

Mice (18-22 months, mean weight ± sd; 34.8 g ± 6.2 g) were randomly assigned a treatment group, anaesthetized with isofluorane and placed on a heated mat to maintain body temperature. Buprenorphine analgesia (0.05 mg/kg, s.c, Vetergesic, Amsterdam) was provided immediately prior to wounding and dorsal hair was removed using a BaByliss trimmer. Nair cream (Church and Dwight, Folkestone, UK) was used to remove the remnants of the dorsal hair to create a surface that the Tegaderm dressing would adhere to. Depilatory cream was carefully removed using PBS and tissue paper to avoid chemical irritation. Claws were trimmed to minimise the potential for scratch-induced skin trauma during the protocol. A single 4 mm excisional wound (Selles Medical, UK) was made to the dorsal skin near the shoulder blades. A suspension of mercaptosuccinic acid (MSA, 400 mg/kg, Sigma-Aldrich) in 40% Pluronic hydrogel was prepared and 25 μl administered topically into the wound. Wounds were dressed with a sterile Tegaderm dressing (3M, Bracknell, UK) which prevented wound contamination, maintained a moist environment and ensured animals would not clean their wounds. Bepanthen Ointment (Bayer, Reading, UK) was applied to the uncovered, depilated skin surrounding the dressing to minimise any irritation.

Mice were individually housed in conventional cages in a 28C warm box throughout the experiment, with additional bedding, which effectively enabled these elderly mice to maintain their body weight. Animals were provided with ‘mash’ (standard chow rehydrated in sterile water) throughout the protocol and were monitored as outlined in Fig. S6. At Day 7 post-wounding, CWs were carefully debrided to remove dead and sloughing tissue. Briefly, mice

were anaesthetized with isoflurane by inhalation, placed on a heated mat and administered Buprenorphine (0.05 mg/kg sc). The existing Tegaderm dressing was carefully removed, ensuring the wound was not pulled in the process. Debridement was performed using 4.25 inch dissection scissors and curved tweezers (Sigma-Aldrich)

Vehicle (PBS) or BMS-470539 (MC1R-Ag) were delivered topically by pipette into the wound cavity immediately after debridement (100 μl in a 30% Pluronic F-127 gel; Sigma Aldrich). Wound areas were calculated using ImageJ software.

Evans Blue assay of lymphatic drainage

Evans blue dye (Sigma-Aldrich, Poole) was dissolved in sterile saline solution to a concentration of 0.5% w/v and 10 μl was injected into the cutaneous wound bed 8 hours prior to cull. The gross appearance of the tissue was recorded using a digital camera immediately following cull. The skin draining lymph nodes (axillary, brachial and inguinal) were then harvested into 200 μl of formamide and incubated for 24 h at 55°C to extract the dye. The tissue pieces were discarded, debris removed via centrifugation and absorbance read in triplicate at 610 nm.

Wound processing

Acute wounds were harvested on days 1, 3, 7, 10 and 14 post-wounding, fixed in 4% PFA (overnight at 4C on a rocker, Sigma Aldrich), washed 3 x 5 min in PBS, transferred to 70% ethanol and then embedded in paraffin. Day 1 and 3 wounds were cut in half using a scalpel and sections (10 μm) taken from the middle of the wound. Day 7, 10 and 14 wounds were sectioned through the wound beyond the midpoint and wound centres identified by staining with Haematoxylin (Gills No.3) and Eosin (Sigma). All CWs were bisected.

Histology

FFPE sections were deparaffinised and rehydrated in: xylene (2 x 3 min), 100% ethanol (2 x 3 nub), 90% ethanol (3 min) and 70% ethanol (3 min). Sections were placed in running tap water before being submerged in haematoxylin (Sigma-Aldrich, Dorset, UK) for 5 s – 1 min depending on staining intensity desired. Excess haematoxylin was rinsed off in tap water twice. Slides were then briefly submerged in acid alcohol (300 ml dH20, 700 ml 100% ethanol, 3 ml concentrated HCL; Sigma-Aldrich), followed by tap water wash. Sections were submerged in eosin (Sigma-Aldrich) for 30 s to provide a counterstain to the haematoxylin. After tap water washes (x 3), sections were dehydrated for mounting in sequential baths of 70%, 90%, 100% ethanol and xylene (x 2) for 30 seconds each. DPX mountant (Sigma-Aldrich) was applied to the sections, followed by a Menzel microscope coverslip (25 x 60 mm, 0.13 mm thick; Thermofisher Scientific, Renfrew, UK). For Picrosirius Red (PSR) staining for collagen, the above protocol was followed but with PSR (0.5 g Sirius Red, 1.3% picric acid in dH2O; Sigma-Aldrich) for 1 hour and no eosin counterstain. For Prussian Blue staining, the above protocol was followed but with Prussian Blue (10% HCl, 5% potassium ferrocyanide in dH2O used rather than haematoxylin.

Immunohistochemistry

Skin sections were deparaffinised and rehydrated as described above. Sections were encircled with a hydrophobic barrier using an ImmEdge pen (Vector labs, Peterborough, UK). Antigen retrieval was carried out using Proteinase K (5 μg/ml, 7 mins, Dako, UK). Sections were rinsed in running tap water for 5 min, blocked (1% BSA, 0.1% Gelatin, 0.5% Triton X-100; Sigma-Aldrich) for 30 min at room temperature. Sections were incubated in primary antibody diluted in block, overnight at 4C in a humidified chamber. After PBS-0.1% Tween-20 wash, an ImmPRESS polymer detection kit was used, followed by a DAB kit, as per the manufacturer's instructions (Vector labs). Sections were counterstained with haematoxylin, dehydrated and mounted as described above.

Microscopy

Tissue sections were imaged on an Axioscan Z1 slide scanner (Zeiss, Cambridge, UK) using the 20x air objective. Immunofluorescence images were taken using a Leica DM2500 microscope, Leica DFC7000 camera and LAS software (Leica Microsystems, GmbH, Milton Keynes, UK), using the 20 x air objective. Numbers of leukocytes per field of view (FOV) were calculated using thresholded 32-bit images and the "analyze particles" function in FIJI software. Blood and lymphatic vessels were quantified by thresholding on fluorescent area in FIJI software.

Collagen alignment

Collagen fibre orientation was desired to be able to identify the level to which wounds recovered their natural structural components during the wound healing process. To undertake this, we developed a MATLAB code which first isolated collagen fibrils from non-fibrous tissue using a colour-based segmentation algorithm. First, the user selected image is converted from an RGB image to a two-dimensional matrix of type $m \times n \times 3$. Where m and n represent the row and column indices respectively. Our code (which we name FIBRAL) converts the image colour space from RGB to L*a*b to more accurately predict small colour differences, key for PSR staining in which small variation detection is required (32). Both the full a-channel and positive range of the b-channel were isolated and superimposed. This new matrix was transformed into grayscale with contrast and brightness increased by 20% and 5% respectively.

To determine the spatial distribution of collagen fibres, a two-dimensional Fourier transformation was performed on the image. This data was transformed from cartesian to polar coordinates by grouping predominant frequency-component orientations of the fibres in 1-degree increments from 0 to 180 degrees. The total intensity at each angle was calculated by summing the grayscale intensity values of each pixel contained within the group. Large

intensity values represented the summation of multiple sinusoidal waves with large amplitude signifying major fibre alignment along the respective orientation. From this data, a comparative analysis can be conducted whereby the dot product was calculated using each permutation of resulting vectors (parallel vectors would provide a dot product of 1, with orthogonal vectors presenting a dot product value of -1). All results were normalised to lie between 0 and 1 with a directionality quotient of 1 representing a parallel field of fibres and a directionality quotient of 0 representing full fibre orientation across all angles in the tissue. The code was validated against images with dominant fibre orientations and combinations thereof. Full details of the coding approach are included in the supplementary material.

Wound Optical Coherence Tomography Angiography

OCTA imaging is a non-invasive imaging method which utilises light to produce cross-sectional images of tissue architecture *in situ* and in real time. This form of imaging allowed the tracking of wound healing parameters such as reepithelialisation within a single mouse over a time course of healing. Additionally OCTA provides information on the perfusion of new blood vessels which cannot be obtained utilising other methods such as immunofluorescence staining.

Equipment used in this study were designed and developed by Professor Zhihong Huang, Dr. Kanheng Zhou, Mr. Yubo Ji and Mr. Duo Zhang (University of Dundee (33,34)). Mice were anaesthetised at the indicated time points place on a heatpad and ultrasound transmission gel (Anagel, Ana Wiz Ltd, Surrey, UK) was applied between the OCT probe and wound to enhance refractive index coupling. A clinical prototype handheld OCTA system was utilised to image dorsal skin wounds. A 200-kHz vertical-cavity surface-emitting swept source laser (5 mW) (SL132120, Thorlabs Inc., Newton, USA) was used as the light source in the system paired with a XY galvo-scanner (6210H, Cambridge technology, Bedford, USA) and a 5X objective lens (LSM03, Thorlabs Inc., Newton, USA). With this configuration, the handheld probe provided a scanning range of 10 × 10 mm2. To generate high resolution 3D OCTA

images for skin architecture and vasculature, the following B-M scanning protocol was applied: Firstly, A-lines were acquired consecutively with a 10 μm interval along the fast scanning axis to generate a B-frame. Each B-frame was then repeated four times at the same location for blood flow extraction. Next, the described repeated B-scans were looped consecutively along the slow scanning axis also with a 10 μm interval to form a complete 3D volume scan. The final volumetric dataset comprised 600 A-lines and 600 cross-sectional planes (2400 B-frames). Data was collected through a customised LabVIEW (NI, Texas, USA) interface for processing.

HMEC-1 culture and transfection

HMEC-1 cells (ATCC: CRL-3243) were cultured in EGM-2 MV (EBM-2 added with growth factors and other supplements, PromoCell). Lipofectamine RNAiMAX (Thermo Fisher Scientific) was used to transfect HMEC-1 with siRNA control or siRNA MC1R oligonucleotides (Qiagen) (20 nM final concentration).

Endothelial Tube Formation Assay

Matrigel (50 µL/well) (BD Matrigel Basement Membrane Matrix, BD Biosciences) was added to the wells in a 96-well plate and allowed to polymerize at 37 °C for 30 min. HMEC-1 cells, an immortalised human microvascular endothelial cell line (35) (15,000 cells) previously transfected with siRNA-control or siRNA MC1R were added to the top of the Matrigel and treated with MC1R agonist BMS-470539. After incubation for 8 hr, tube formation was assessed by acquiring four randomly microscopic fields (magnification ×10) by using Nikon Eclipse Ti inverted microscope. Total tube length and branching points were assessed by Angiogenesis Analyzer for ImageJ analysis software (36). For confocal imaging, cells were fixed (4% PFA, 15 m), blocked ( ) and stained (phalloidin, ; DAPI,)

Human Tissue

FFPE sections of human CWs were provided by NHS Lothian Tissue Bank (ethical approval: 15/ED/0094) with approval from the Tissue Governance Committee (2017/0023/SR736). Inclusion criteria were pressure ulcers, diabetic foot ulcers and venous leg ulcers from male and female donors over 50 years of age. Exclusion criteria were patients with cancer, pressure ulcers from patients with diabetes. Prior to receipt, all samples were anonymised.

Statistical analysis Student's *t*-test, one-way and two-way ANOVA with Bonferroni's multiple comparison test were performed using GraphPad Prism 9.0 software and detailed in the respective Figure legends.

Diagrams Biorender was used to create the schematics in Figures 1, 5 and 6.

Acknowledgments: We acknowledge the support of the QMRI SURF facilities for histological services and BVS (Bioresearch and Veterinary Services), especially Dr Nacho Vinuela-Fernandez for assistance with animal studies. We thank Professor Ian Jackson for providing the MC1Re/e mouse line and Dr Andrew Tambyraja and Professor Keith Harding for helpful insights on CWs from a clinical perspective and Professor Paul Martin for general discussions. We thank Dr Alison Munro of the Institute of Genetics and Cancer (IGC) for running nanostring assays, Wolfson Bioimaging Facility for assistance with Incucyte experiments and Dr Matthieu Vermeren (CALM services) for microscopy input. Thanks also to Prof Stuart Forbes, Prof David Dockrell and Prof Julia Dorin for mentorship.

Funding: This work was funded by a Sir Henry Dale Fellowship (202581/Z/16/Z), Elizabeth Blackwell Early Career Fellowship (Wellcome ISSF) and a University of Edinburgh Chancellors Fellowship awarded to Dr Jenna L Cash. Dr Holly Rocliffe was supported with a

Chancellors Fellowship PhD Studentship. Work in MC lab was funded by an EPSRC New Investigator grant EP/S019847/1 and CB is funded by a Carnegie Trust for Scotland PhD studentship.

Contributions: HR and SAW performed experiments, analysed the data and wrote the manuscript. GK and AP performed experiments and analysed the data. YN performed histology and histological analysis of skin wounds. KZ and YJ performed OCT imaging and analysis under the supervision of ZH. CB, YC and MC developed FIBRAL. AP performed experiments and analysed data. TZ performed vessel width analysis. AB provided expert advice as an inflammatory dermatopathologist. AC advised on the design and execution of *in vitro* angiogenesis experiments, performed and analysed these experiments. JLC conceived and planned the project, performed the experiments, analysed and interpreted the data, wrote the manuscript, obtained funding, and supervised the project.

References

1. Cash JL, Martin P. Myeloid Cells in Cutaneous Wound Repair. 2016;17.

2. Rodrigues M, Kosaric N, Bonham CA, Gurtner GC. Wound Healing: A Cellular Perspective. Physiological Reviews. 2019 Jan 1;99(1):665–706.

3. Sen CK, Gordillo GM, Roy S, Kirsner R, Lambert L, Hunt TK, et al. Human skin wounds: A major and snowballing threat to public health and the economy. Wound Repair and Regeneration. 2009 Nov;17(6):763–71.

4. Olsson M, Järbrink K, Divakar U, Bajpai R, Upton Z, Schmidtchen A, et al. The humanistic and economic burden of chronic wounds: A systematic review: The burden of chronic wounds. Wound Rep and Reg. 2019 Jan;27(1):114–25.

5. Frykberg RG, Banks J. Challenges in the Treatment of Chronic Wounds. Advances in Wound Care. 2015 Sep;4(9):560–82.

6. Nunan R, Harding KG, Martin P. Clinical challenges of chronic wounds: searching for an optimal animal model to recapitulate their complexity. Disease Models & Mechanisms. 2014 Nov 1;7(11):1205–13.

7. Zindle JK, Wolinsky E, Bogie KM. A review of animal models from 2015 to 2020 for preclinical chronic wounds relevant to human health. Journal of Tissue Viability. 2021 Aug;30(3):291–300.

8. Nussbaum SR, Carter MJ, Fife CE, DaVanzo J, Haught R, Nusgart M, et al. An Economic Evaluation of the Impact, Cost, and Medicare Policy Implications of Chronic Nonhealing Wounds. Value in Health. 2018 Jan;21(1):27–32.

9. Moore K, Huddleston E, Stacey MC, Harding KG. Venous leg ulcers ? the search for a prognostic indicator. Int Wound Journal. 2007 Jun;4(2):163–72.

10. Goh OQ, Ganesan G, Graves N, Ng YZ, Harding K, Tan KB. Incidence of chronic wounds in Singapore, a multiethnic Asian country, between 2000 and 2017: a retrospective cohort study using a nationwide claims database. BMJ Open. 2020 Sep;10(9):e039411.

11. Muffley LA, Zhu KQ, Engrav LH, Gibran NS, Hocking AM. Spatial and Temporal Localization of the Melanocortin 1 Receptor and Its Ligand α–Melanocyte-Stimulating Hormone during Cutaneous Wound Repair. J Histochem Cytochem. 2011 Mar;59(3):278–88.

12. Denat L, Kadekaro AL, Marrot L, Leachman SA, Abdel-Malek ZA. Melanocytes as Instigators and Victims of Oxidative Stress. Journal of Investigative Dermatology. 2014 Jun;134(6):1512–8.

13. Valverde P, Healy E, Jackson I, Rees JL, Thody AJ. Variants of the melanocyte–stimulating hormone receptor gene are associated with red hair and fair skin in humans. Nat Genet. 1995 Nov;11(3):328–30.

14. Sood RF, Hocking AM, Muffley LA, Ga M, Honari S, Reiner AP, et al. Race and Melanocortin 1 Receptor Polymorphism R163Q Are Associated with Post-Burn Hypertrophic Scarring: A Prospective Cohort Study. Journal of Investigative Dermatology. 2015 Oct;135(10):2394–401.

15. Leoni G, Voisin MB, Carlson K, Getting S, Nourshargh S, Perretti M. The melanocortin MC1 receptor agonist BMS-470539 inhibits leucocyte trafficking in the inflamed vasculature:

Melanocortins control vascular inflammation. British Journal of Pharmacology. 2010 May;160(1):171–80.

16. Lorenz J, Seebach E, Hackmayer G, Greth C, Bauer RJ, Kleinschmidt K, et al. Melanocortin 1 Receptor-Signaling Deficiency Results in an Articular Cartilage Phenotype and Accelerates Pathogenesis of Surgically Induced Murine Osteoarthritis. Malaval L, editor. PLoS ONE. 2014 Sep 5;9(9):e105858.

17. Cash JL, Bass MD, Campbell J, Barnes M, Kubes P, Martin P. Resolution Mediator Chemerin15 Reprograms the Wound Microenvironment to Promote Repair and Reduce Scarring. Current Biology. 2014 Jun;24(12):1406–14.

18. Potente M, Gerhardt H, Carmeliet P. Basic and Therapeutic Aspects of Angiogenesis. Cell. 2011 Sep;146(6):873–87.

19. Renò F, Sabbatini M. Breaking a Vicious Circle: Lymphangiogenesis as a New Therapeutic Target in Wound Healing. Biomedicines. 2023 Feb 21;11(3):656.

20. Güç E, Briquez PS, Foretay D, Fankhauser MA, Hubbell JA, Kilarski WW, et al. Local induction of lymphangiogenesis with engineered fibrin-binding VEGF-C promotes wound healing by increasing immune cell trafficking and matrix remodeling. Biomaterials. 2017 Jul;131:160–75.

21. Paavonen K, Puolakkainen P, Jussila L, Jahkola T, Alitalo K. Vascular Endothelial Growth Factor Receptor-3 in Lymphangiogenesis in Wound Healing. The American Journal of Pathology. 2000 May;156(5):1499–504.

22. Rutkowski JM, Boardman KC, Swartz MA. Characterization of lymphangiogenesis in a model of adult skin regeneration. American Journal of Physiology-Heart and Circulatory Physiology. 2006 Sep;291(3):H1402–10.

23. Gurevich DB, Severn CE, Twomey C, Greenhough A, Cash J, Toye AM, et al. Live imaging of wound angiogenesis reveals macrophage orchestrated vessel sprouting and regression. EMBO J [Internet]. 2018 Jul 2 [cited 2022 Nov 28];37(13). Available from: https://onlinelibrary.wiley.com/doi/10.15252/embj.201797786

24. Dhall S, Do D, Garcia M, Wijesinghe DS, Brandon A, Kim J, et al. A Novel Model of Chronic Wounds: Importance of Redox Imbalance and Biofilm-Forming Bacteria for Establishment of Chronicity. Appanna VD, editor. PLoS ONE. 2014 Oct 14;9(10):e109848.

25. Dhall S, Do DC, Garcia M, Kim J, Mirebrahim SH, Lyubovitsky J, et al. Generating and Reversing Chronic Wounds in Diabetic Mice by Manipulating Wound Redox Parameters. Journal of Diabetes Research. 2014;2014:1–18.

26. Guest JF, Fuller GW, Vowden P. Cohort study evaluating the burden of wounds to the UK's National Health Service in 2017/2018: update from 2012/2013. BMJ Open. 2020 Dec;10(12):e045253.

27. McDougall S, Dallon J, Sherratt J, Maini P. Fibroblast migration and collagen deposition during dermal wound healing: mathematical modelling and clinical implications. Phil Trans R Soc A. 2006 Jun 15;364(1843):1385–405.

28. Caley MP, Martins VLC, O'Toole EA. Metalloproteinases and Wound Healing. Advances in Wound Care. 2015 Apr;4(4):225–34.

29. Zomer HD, Trentin AG. Skin wound healing in humans and mice: Challenges in translational research. Journal of Dermatological Science. 2018 Apr;90(1):3–12.

30. Jiang D, Christ S, Correa-Gallegos D, Ramesh P, Kalgudde Gopal S, Wannemacher J, et al. Injury triggers fascia fibroblast collective cell migration to drive scar formation through N-cadherin. Nat Commun. 2020 Dec;11(1):5653.

31. Prescott MJ, Lidster K. Improving quality of science through better animal welfare: the NC3Rs strategy. Lab Anim. 2017 Apr;46(4):152–6.

32. Bora DJ, Gupta AK, Khan FA. Comparing the Performance of L*A*B* and HSV Color Spaces with Respect to Color Image Segmentation [Internet]. arXiv; 2015 [cited 2022 Nov 28]. Available from: http://arxiv.org/abs/1506.01472

33. Ji Y, Yang S, Zhou K, Lu J, Wang R, Rocliffe HR, et al. Semisupervised representative learning for measuring epidermal thickness in human subjects in optical coherence tomography by leveraging datasets from rodent models. J Biomed Opt [Internet]. 2022 Aug 19 [cited 2022 Nov 29];27(08). Available from: https://www.spiedigitallibrary.org/journals/journal-of-biomedical-optics/volume-27/issue-08/085002/Semisupervised-representative-learning-for-measuring-epidermal-thickness-in-human-subjects/10.1117/1.JBO.27.8.085002.full

34. Ji Y, Yang S, Zhou K, Rocliffe HR, Pellicoro A, Cash JL, et al. Deep-learning approach for automated thickness measurement of epithelial tissue and scab using optical coherence tomography. J Biomed Opt [Internet]. 2022 Jan 18 [cited 2022 Nov 29];27(01). Available from: https://www.spiedigitallibrary.org/journals/journal-of-biomedical-optics/volume-27/issue-01/015002/Deep-learning-approach-for-automated-thickness-measurement-of-epithelial-tissue/10.1117/1.JBO.27.1.015002.full

35. Ades EW, Candal FJ, Swerlick RA, George VG, Summers Susan, Bosse DC, et al. HMEC-1: Establishment of an Immortalized Human Microvascular Endothelial Cell Line. Journal of Investigative Dermatology. 1992 Dec;99(6):683–90.

36. Carpentier G, Berndt S, Ferratge S, Rasband W, Cuendet M, Uzan G, et al. Angiogenesis Analyzer for ImageJ — A comparative morphometric analysis of “Endothelial Tube Formation Assay” and “Fibrin Bead Assay”. Sci Rep. 2020 Dec;10(1):11568.

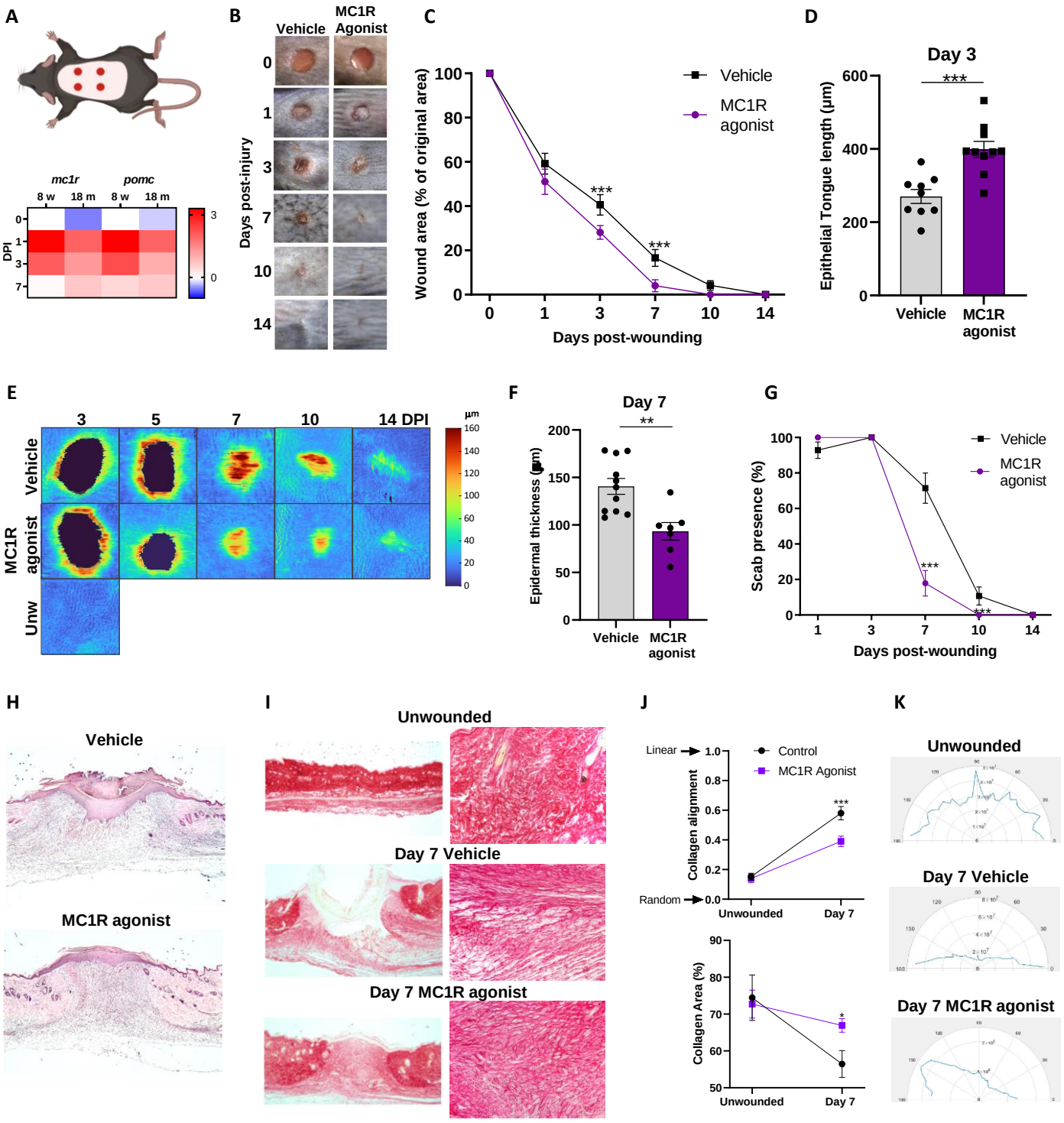

Figure 1 – MC1R drives wound healing with reduced scarring

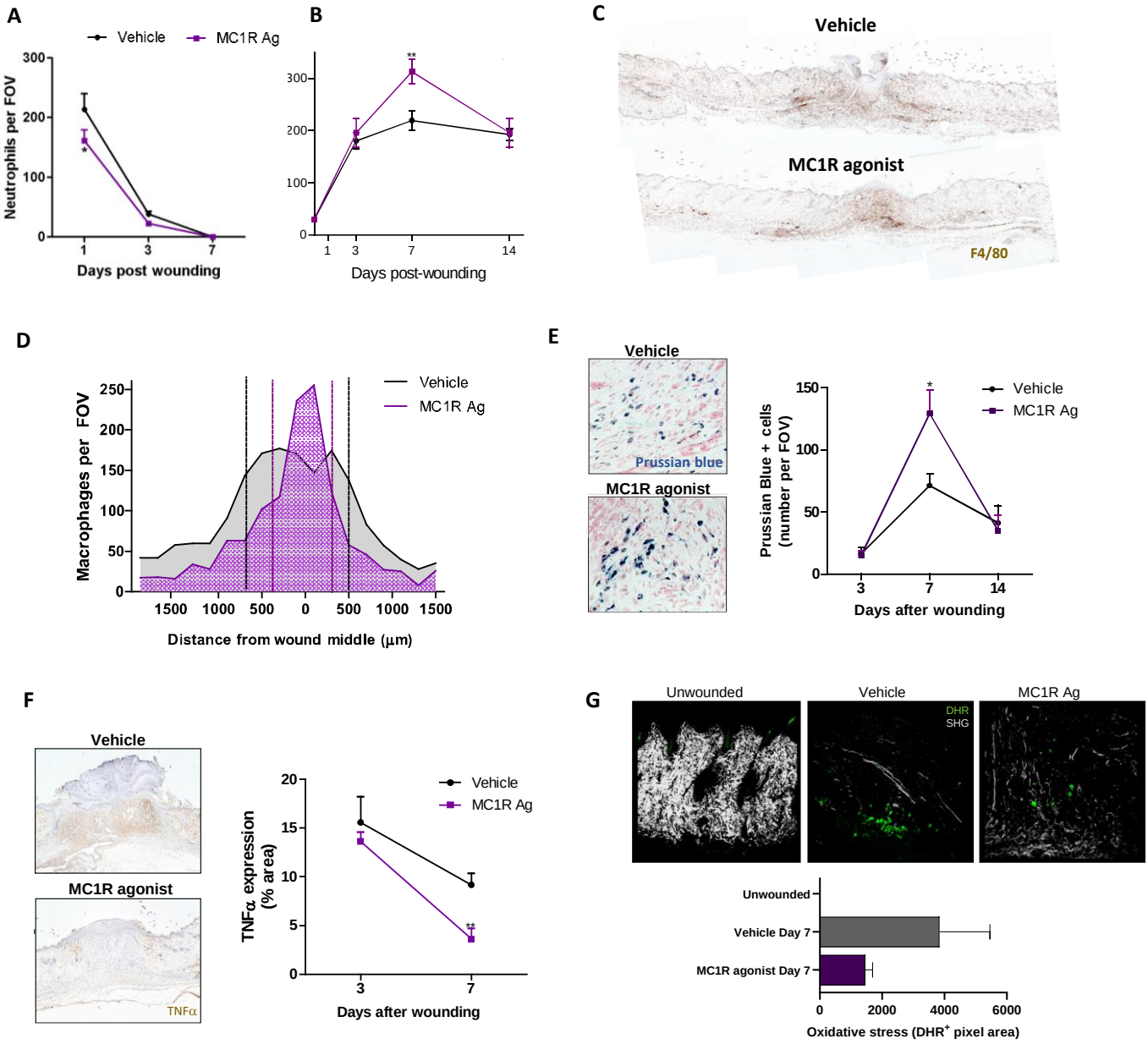

Figure 2 – MC1R agonist modulates wound microenvironment

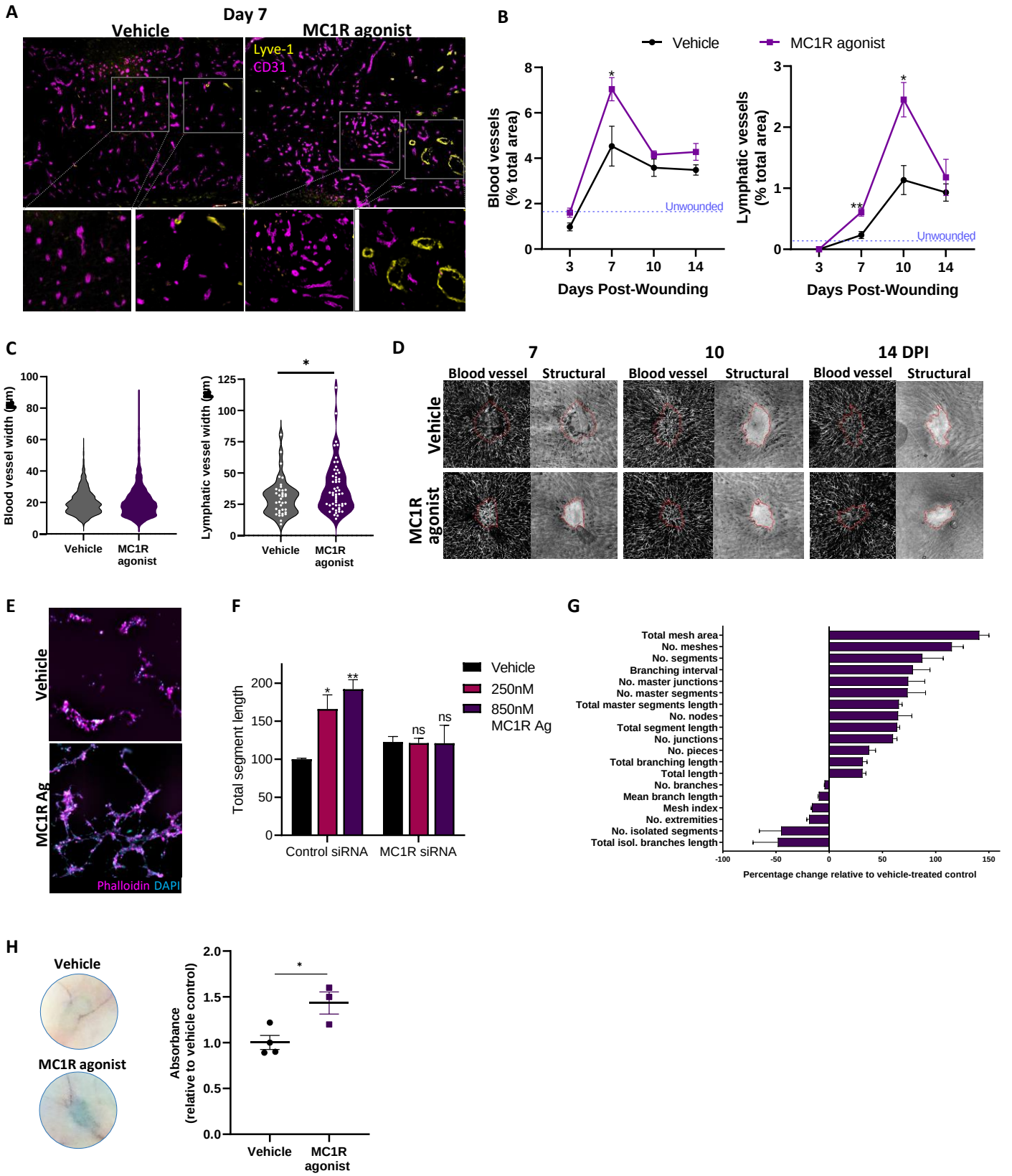

Figure 3 – MC1R agonist drives wound angiogenesis and lymphangiogenesis

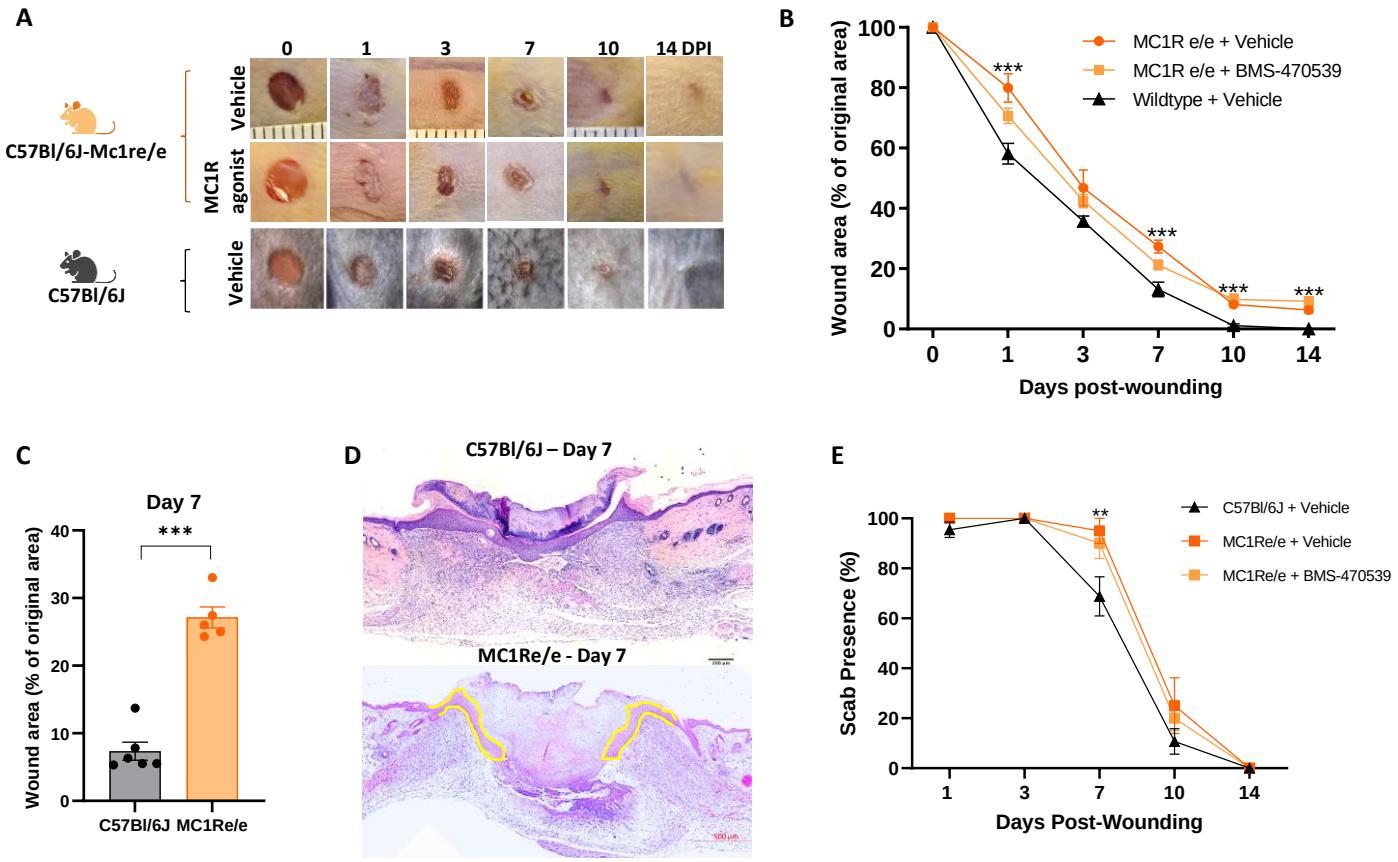

Figure 4 - Lack of functional MC1R impairs acute wound healing

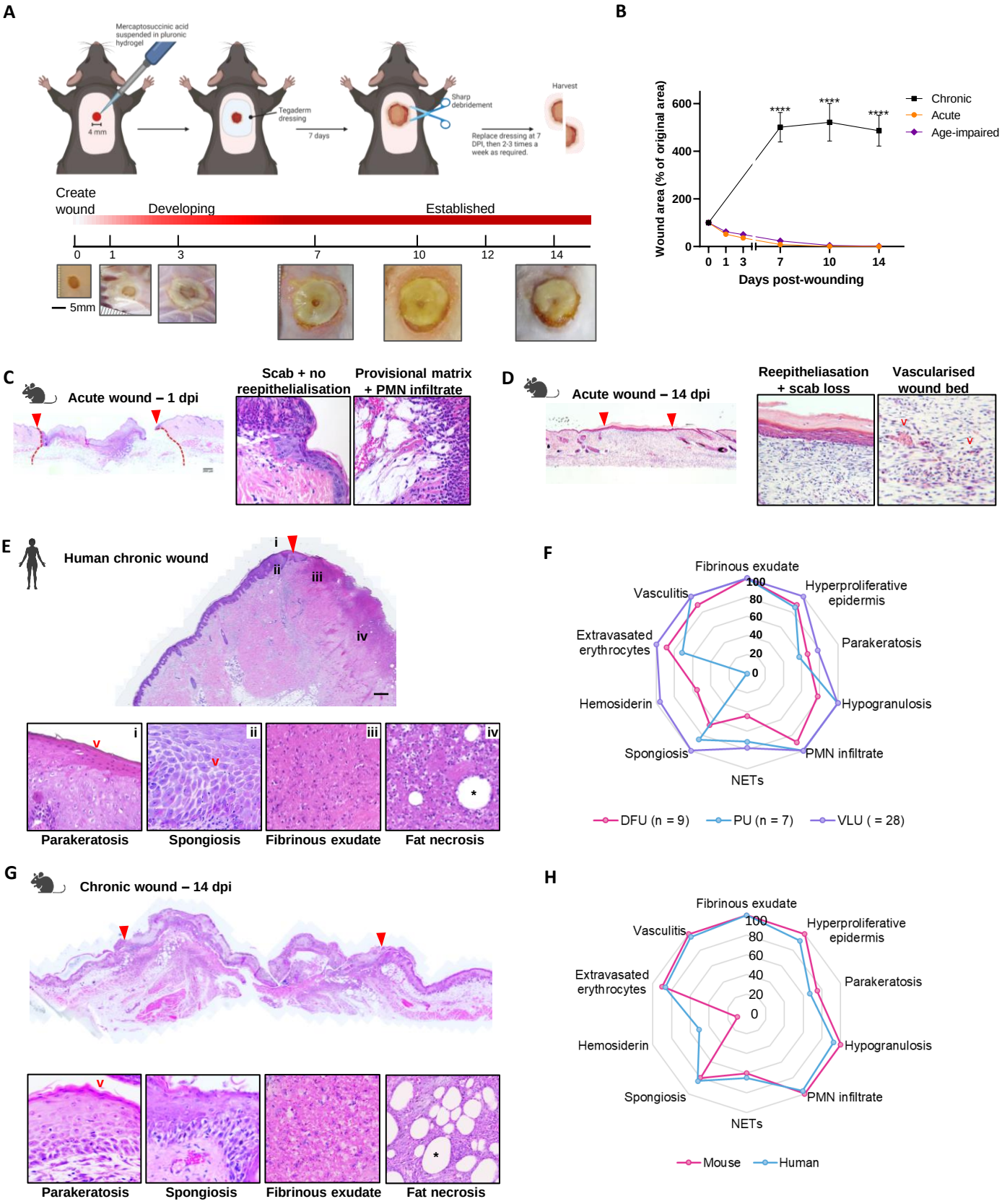

Figure 5 – Preclinical model recapitulates hallmarks of human chronic wounds

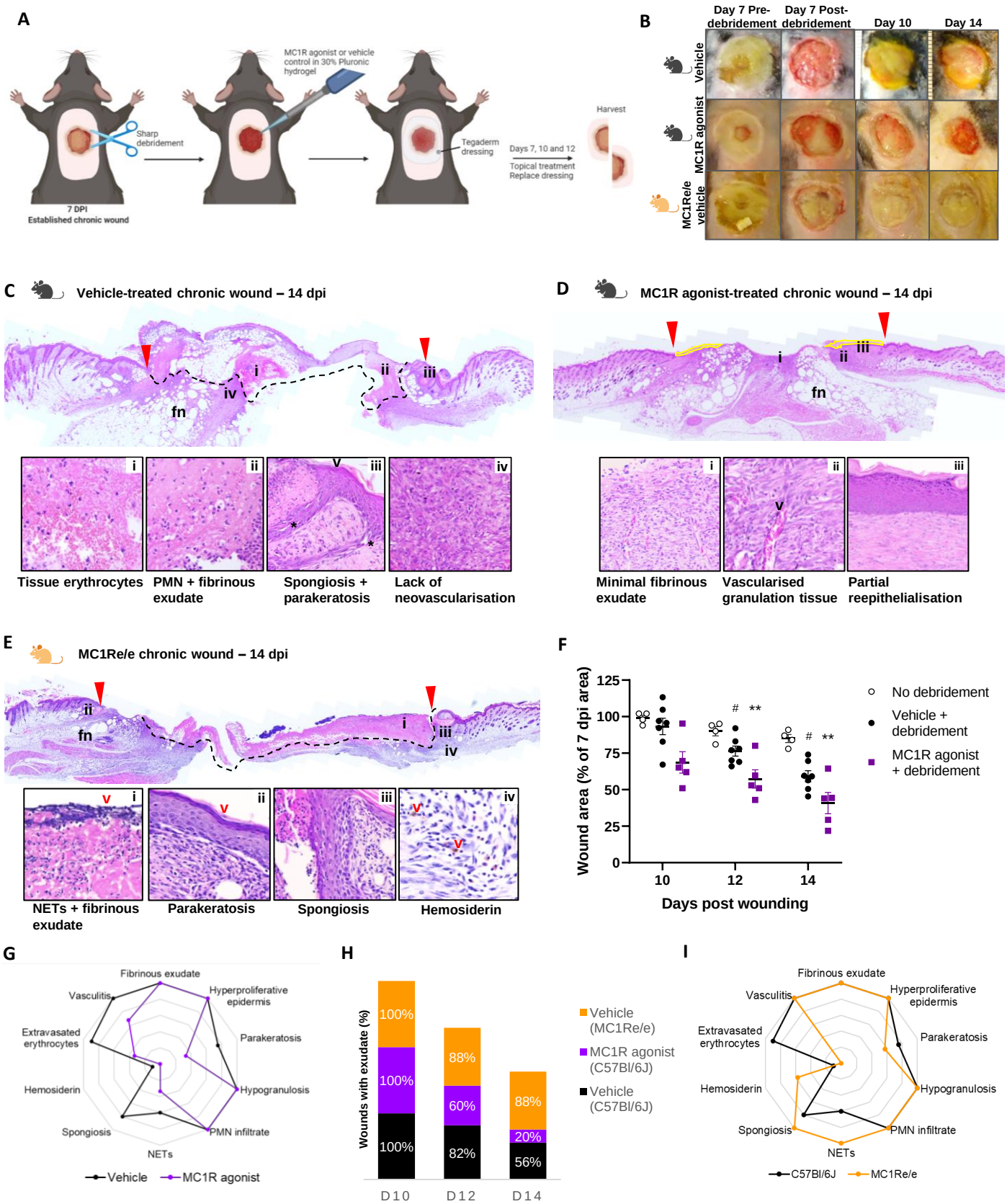

Figure 6 - MC1R agonist rescues the healing response in a preclinical chronic wound model

FIGURE S1 – FIBRAL MANUAL

A. GENERAL INFORMATION

1.1 System Overview

FIBRAL is an image processing tool which runs parallel to MATLAB to determine fibre orientation within soft tissue structures. By offering an easy to use and user-friendly interface, FIBRAL can be applied without the prerequisite of previous MATLAB programming knowledge.

FIBRAL is capable of performing the following operations:

- Image acquisition using the built-in windows folder and file manager
- Colour space alteration and segmentation
- Image filtering to remove noise after segmentation
- Detection of fibre orientation
- Displaying results in the form of a histogram and both a linear and polar plot
- Calculation of overall “directionality coefficient” to provide single point metric of alignment

1.2 System Requirements

As a direct result of utilising built-in MATLAB toolboxes, the only existing requirements are that of MATLAB version R2018a and above. At the time of writing this document, 28/11/2022, the minimum requirements to run MATLAB are:

- Windows 7 or above
- Any Intel or AMD processor with four logical cores
- 22GB of storage space
- 4GB RAM

- Image Analysis Toolbox

B. USER INTERFACE

2.1 An Introduction to the FIBRAL User Interface

FIBRAL offers users a simple to use interface, with minimised user inputs to give users an efficient semi-autonomous system. An example of the blank user interface experienced upon opening, and the user interface showing results of a processed image are shown on the following two pages.

FIBRAL is capable of reading .png, .tif, .jpg and .bmp image files. However, further data formats can be included as and when required.

Number	Function
1	Displays the selected image
2	Allows user to skip segmentation steps if wanting to rerun a previously segmented image
3	Allows user to select image for analysis using standard OS file browser
4	User copies file path for data saving here
5	This button is used to confirm the chosen file path
6	Begins image analysis sequence
7	Displays segmented image
8	Displays alignment index
9	Displays polar plot
10	Displays histogram and linear plot

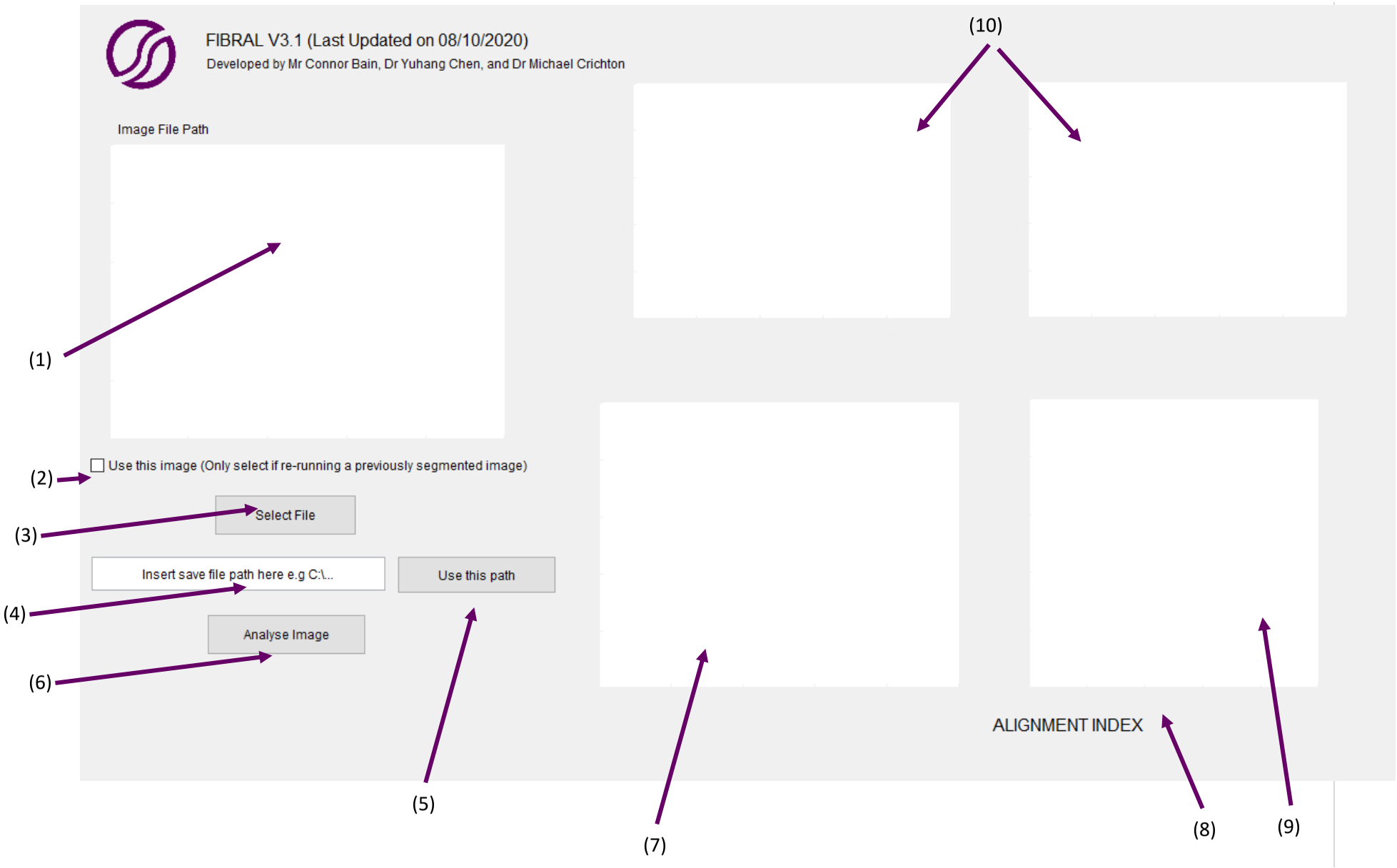
FIBRAL V3.1 (Last Updated on 08/10/2020)
Developed by Mr Connor Bain, Dr Yuhang Chen, and Dr Michael Crichton
Image File Path
Use this image (Only select if re-running a previously segmented image)
Select File
Insert save file path here e.g C:\...
Use this path
Analyse Image
ALIGNMENT INDEX
(1)
(2)
(3)
(4)
(5)
(6)
(7)
(8)
(9)
(10)

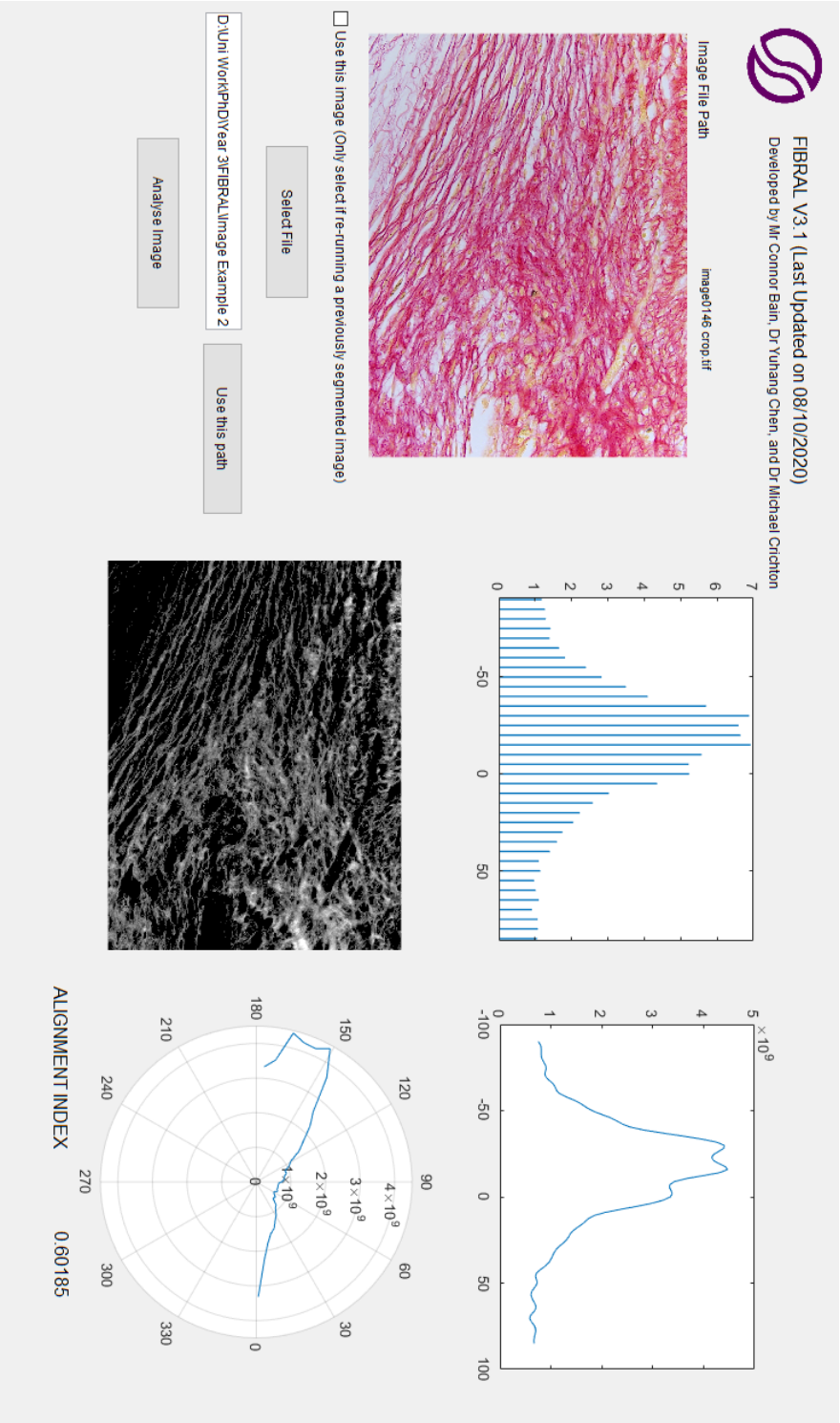

Figure 1 – User interface after successful completion of tissue analysis

C. DEMONSTRATION OF CODE

3.1 Example 1 – Unwounded Tissue – BW Image

The following example will demonstrate how FIBRAL can be used to analyse fibrous tissue, without the requirement of image segmentation and filtering. This is useful when analysing a black and white image, or when wanting to rerun a previously processed image.

1. To open FIBRAL double click the GUI2.m file from your file explorer:

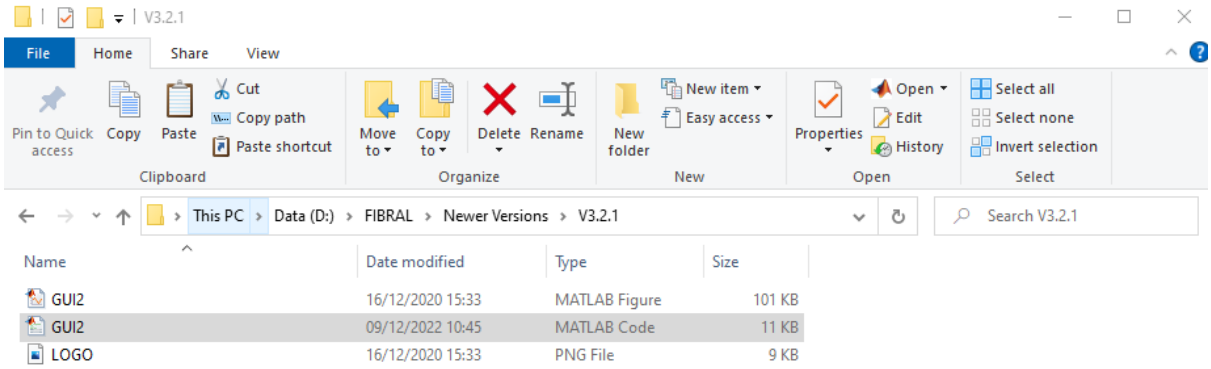

2. Once opened you should be presented with the following code window:

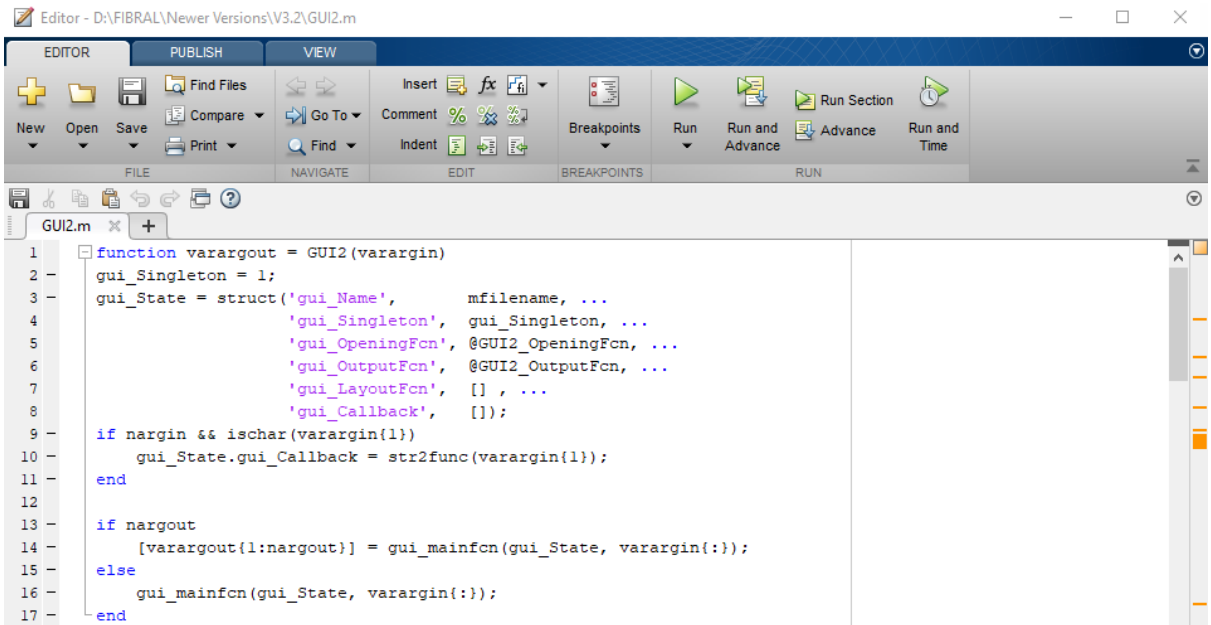

3. To run FIBRAL, click the green “run” arrow

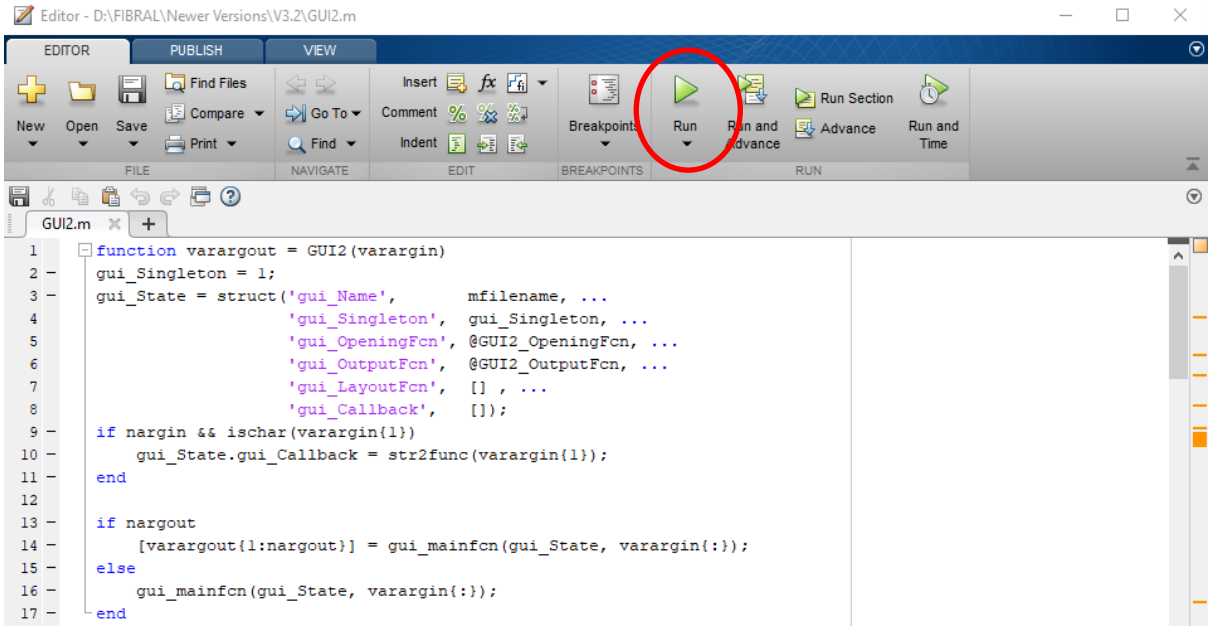

4. You should now be presented with a blank FIBRAL GUI

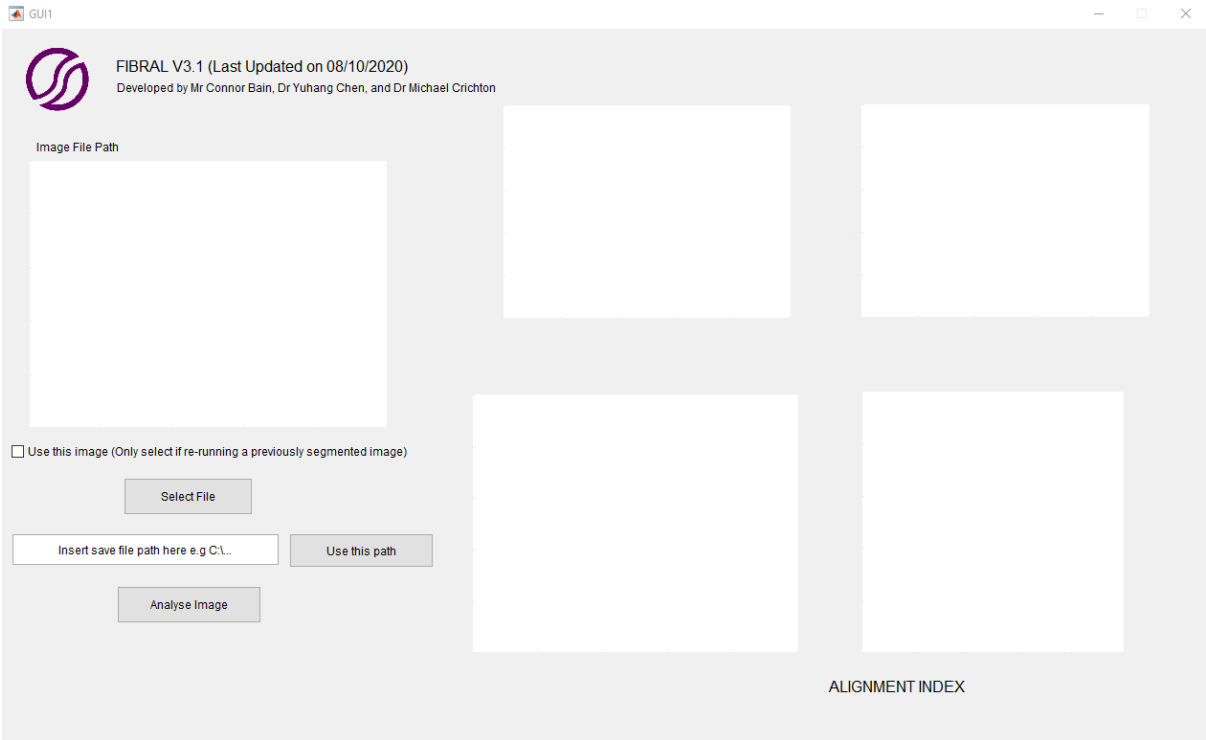

5. To open the image for analysis, click the button labelled ‘Select File’

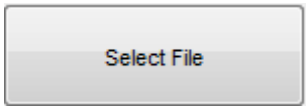

6. Navigate to the folder where the example images are saved and select the file ‘Example1.png’

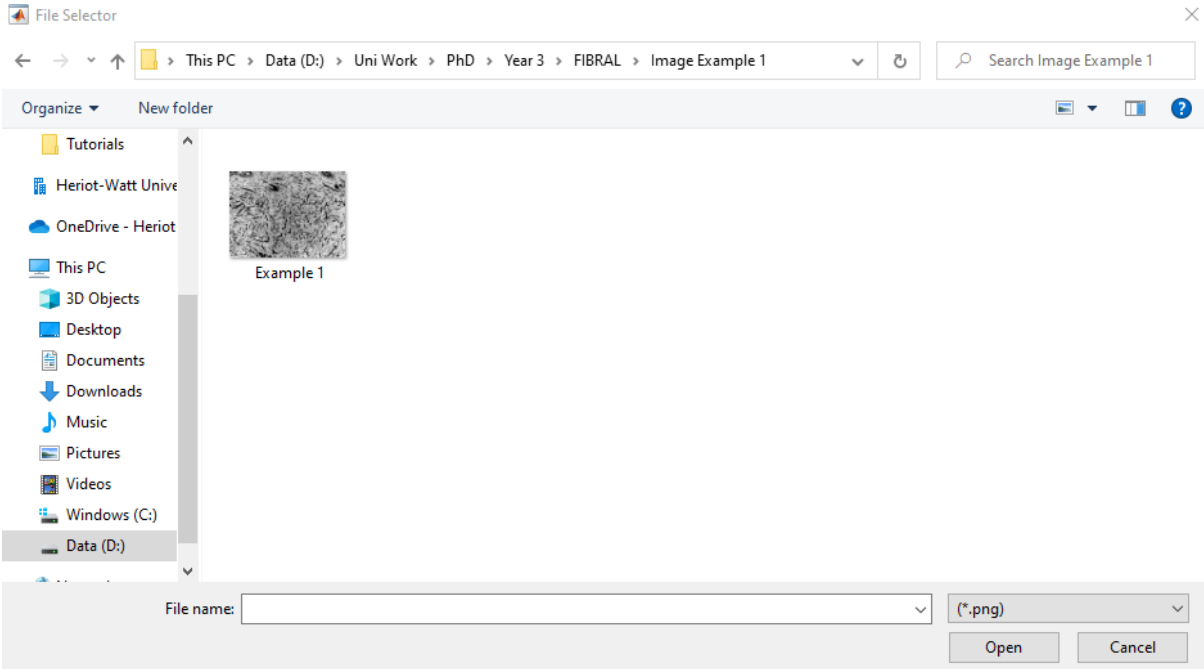

The following should now be shown on the user interface

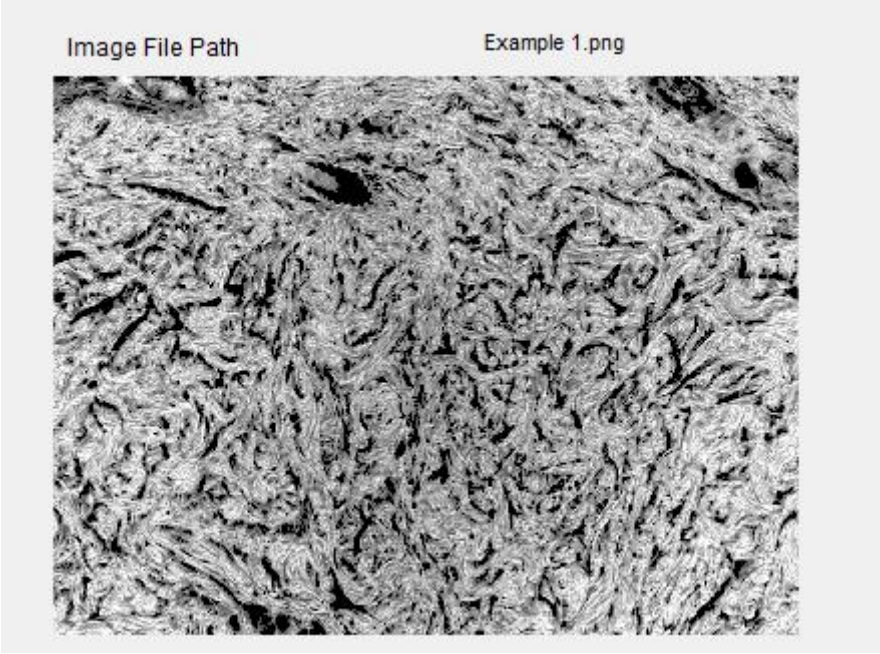

7. Tick the checkbox under the displayed image

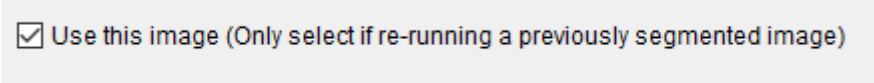

8. Paste a save path into the dialog box and press the “use this path” button

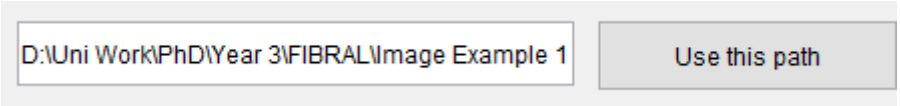

9. Select the button labelled ‘Analyse Image’. You should now be presented with the following screen:

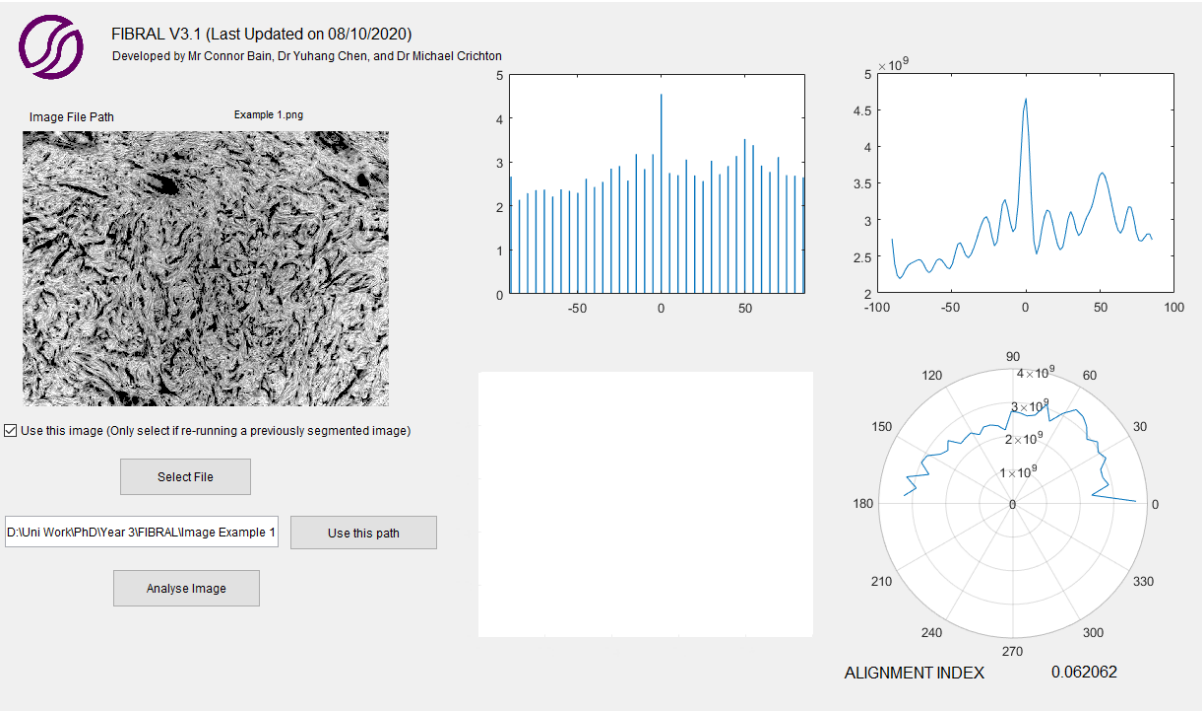

The following graphs should now be displayed on the interface. It can be noted from these graphs, that the no major angle of orientation is found. This is best represented with the polar plot and alignment index value which presents a value of 0.062. The code saves the following files into the chosen directory:

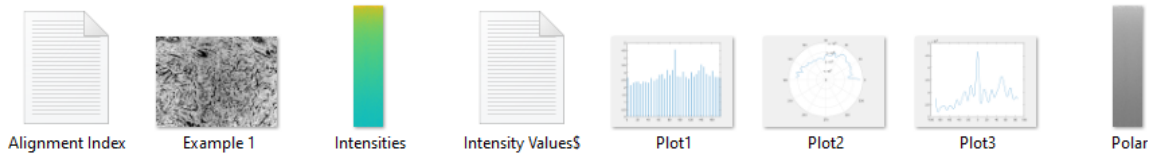

The “Intensities” and “Polar” image files contain the pixel data obtained from the 2D FFT and subsequent polar coordinate conversion algorithms. The histogram, linear plot and polar plot is saved as a .png file. The “Intensity Values” .txt file contains the intensity data at each 5 degree bin, allowing for recreation of the aforementioned plots in the user’s preferred data analysis software. The “Alignment Index” .txt stores the overall alignment coefficient calculated during analysis.

3.2 Example 2 – PSR Stained Wounded Tissue

The following example will demonstrate how FIBRAL can be used to analyse histological slides, such as those used for wound healing monitoring

1. Run FIBRAL and click the button labelled 'Select File'

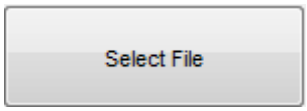

2. Navigate to the folder 'FIBRAL/Images' and select the file 'Example2.png'

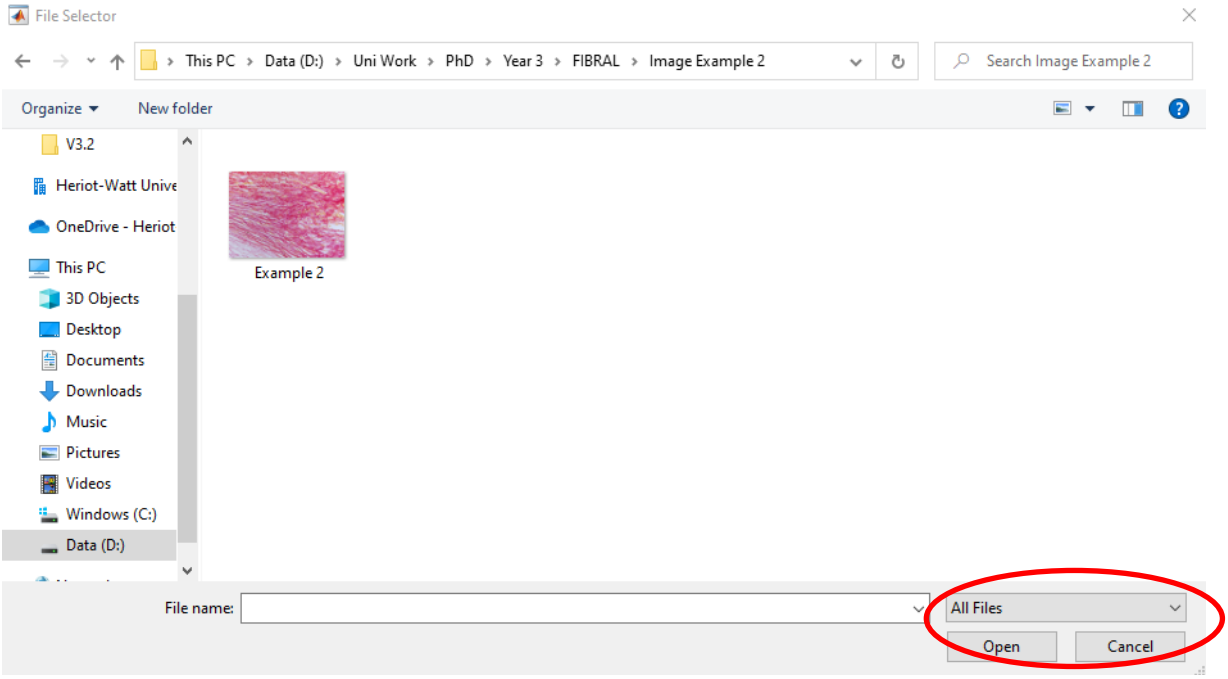

In the case of example 2, the image is not a png. In this instance you need to change the drop down menu (highlighted above in red) from ".png" to "All Files".

The following should now be shown on the user interface

3. Paste a save path into the dialog box and press the “use this path” button

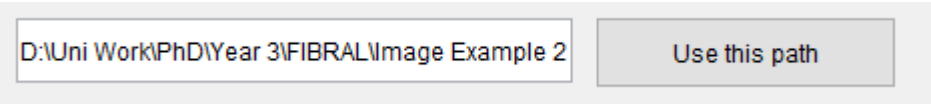

4. Now press the “Analyse Image” button. Doing so should present you with the following screen:

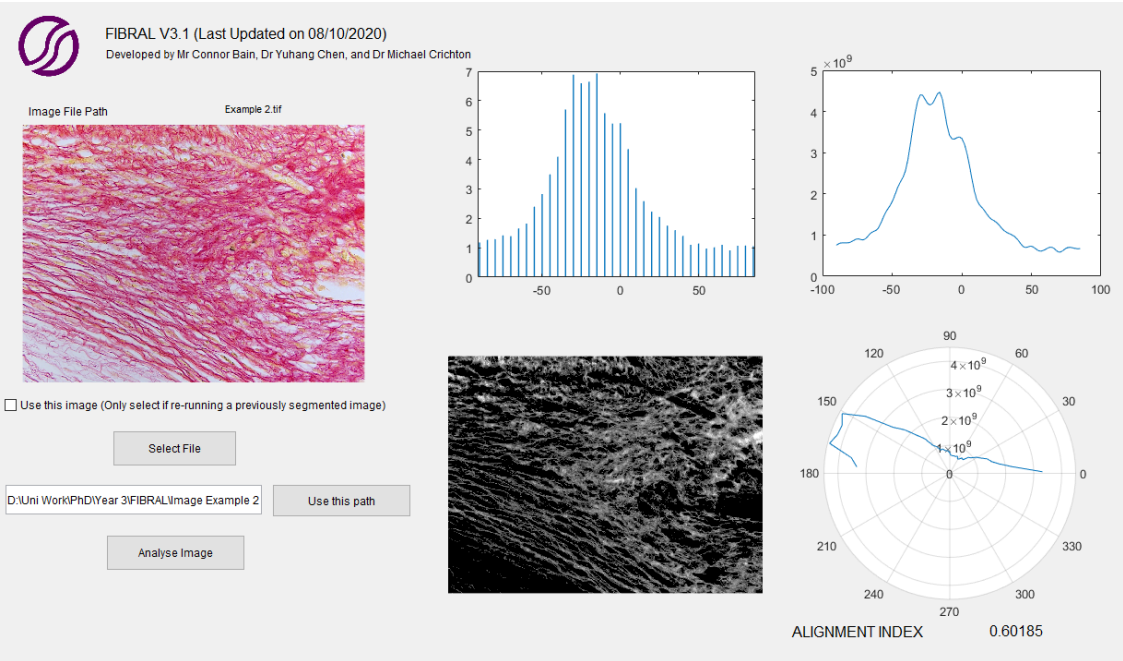

This image presents a primary angle of orientation (around 160±10° from the horizontal). This is reflected in the alignment index value of 0.602; significantly higher than that seen in the previous example.

When analysing a colour image, two extra images are saved:

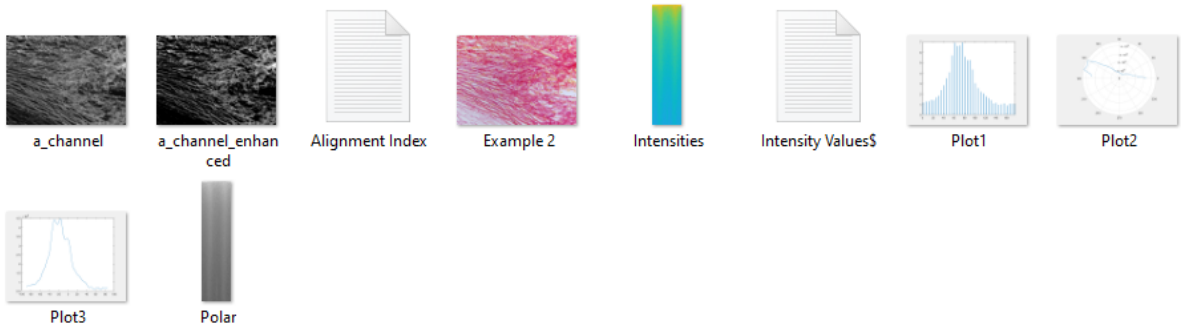

The file named “a_channel” shows the colour segmented image containing the a-channel superimposed with the +ve region of the b-channel (described in the methodology). The file named “a_channel_enhanced” shows the final image used for analysis after colour and contrast adjustments have been made, with subsequent island size removal algorithms run.

3.3 Explanation of Results Obtained During FIBRAL Analysis

During analysis, FIBRAL records and export a variety of parameters which are used to understand the overall global distribution of fibres in an image. Firstly, a linear plot and histogram is generated similar to that shown below:

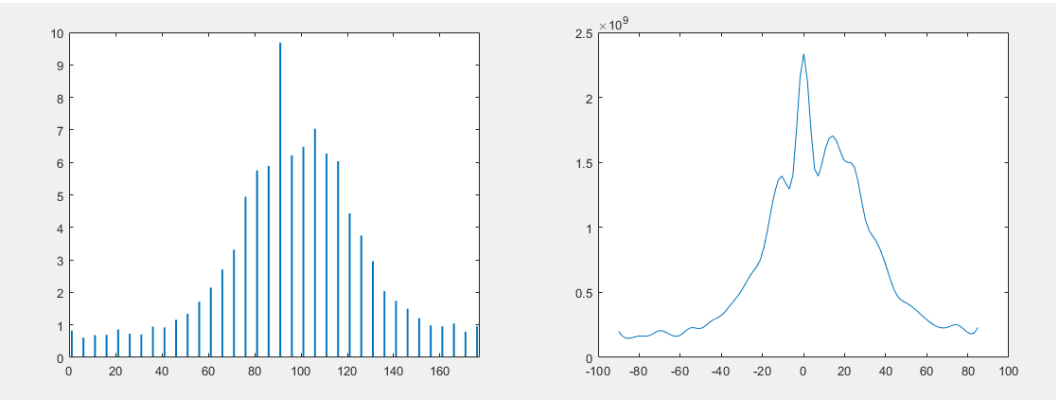

In the case of the linear plot, the x-axis denotes the angular orientation of fibres where 0 degrees denotes the horizontal plane, with 90 degrees denoting the vertical plane. The histogram presents similar data however the results are translated by 90 degrees where 0 degrees denotes the vertical plane. The y-axis in both plots is linked to the overall pixel intensity at each angle of distribution. Data here is obtained from the polar conversion of the adapted image. A continuous curve is displayed in the linear plot with the histogram outlining data summed in 5 degree bin sizes and normalised to a value between 0 and 10. In both cases, it is apparent that we observe a primary distribution of fibres along the horizontal plane with a deviation of approximately ±15 degrees.

To better visualise the distribution of these fibres, FIBRAL exports the linear plot data in the form of a polar plot.

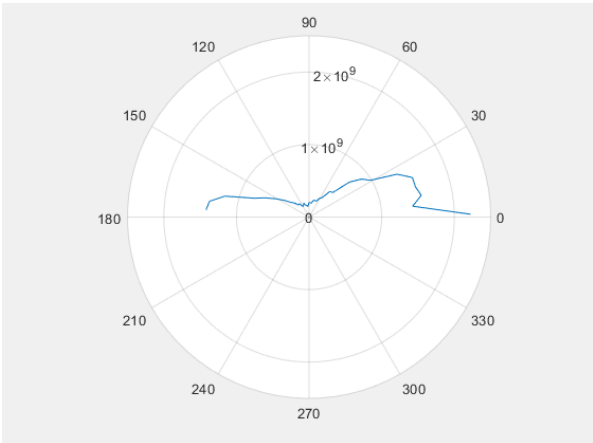

Polar plots are used to provide better visualisation of the fibre distributions in an image. It should be noted that in all plots, the intensity value obtained is related to the overall pixel intensity at each

integer angle; not a quantification of the number of fibres in an image. Hence, the absolute intensity values of various images may different due to variations in contrast and brightness, but the overall distribution characteristics remain consistent. To combine results among data sets for further analysis, it is advised that the user utilises a basic scaling algorithm to set all data sets to the same threshold value. Note, using a normalisation algorithm is not advised as this will greatly skew the data in cases where a non-linear distribution is observed. The intensity plot values are saved to a .txt file to allow the user to recreate the polar and linear plots using their preferred data presentation software.

The primary metric used to identify the level of alignment observed in an image is known as the "alignment index". This value is calculated in FIBRAL and exported into a .txt file. To generate a quantifiable metric which describes the level of anisotropy present in a collagen fibre matrix a two-dimensional array is created which stores the overall intensity value at each one-degree bin size:

$$\theta_{ij} = \begin{bmatrix} \alpha_1 & \alpha_2 & \dots & \alpha_{180} \\ I_1 & I_2 & \dots & I_{180} \end{bmatrix}$$

Where α and I relate to the angle and intensity values at each 1 degree bin size. To analyse the directionality of the fibre distribution, we create a direction vector at each 1 degree bin size with a magnitude equivalent to the summed intensity value of the pixels:

$$\begin{bmatrix} x \\ y \end{bmatrix} = \begin{Bmatrix} I_{ij} \times \cos\alpha \\ I_{ij} \times \sin\alpha \end{Bmatrix}$$

From this, a comparative analysis can be conducted whereby the dot product is calculated using ach permutation of two vectors:

$$d_{ij} = \frac{v_i . v_j}{|v_i||v_j|}$$

Therefore, it is apparent that parallel vectors would provide a dot product of 1, with orthogonal vectors presenting a dot product value of -1. After completion of the above phase, all results are normalised such that they lie between 0 and 1. All N segments can then be averaged to give an overall directionality quotient:

$$d = \frac{\sum_{i=1}^{i=N} \frac{\sum_{j=1}^{j=N}}{N}}{N}$$

A directionality quotient of 1 represents an ideally linear case, where all fibres are oriented along one angle. Whereas a directionality quotient of 0 represents ideal isotropy where an equal proportion of fibres are oriented across all angles.

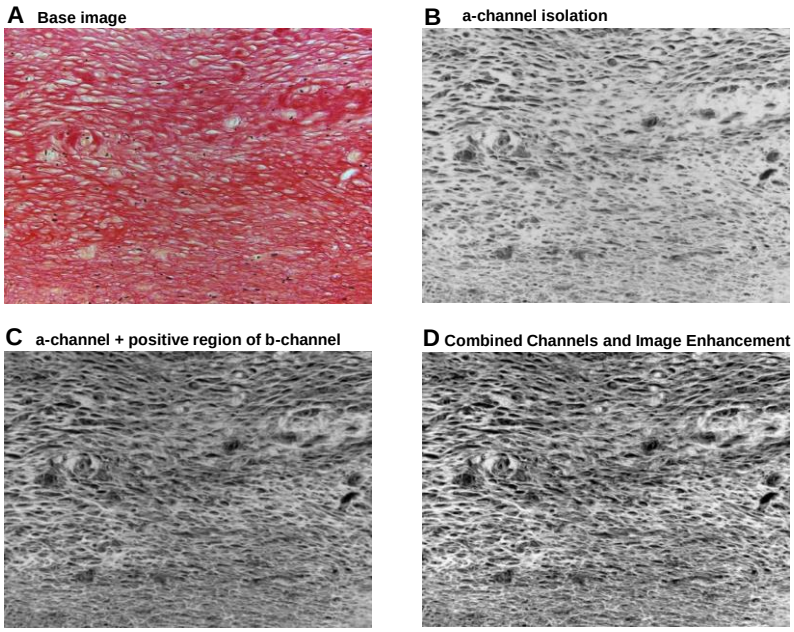

Figure S2 Progression of image preparation algorithm showing improved fibre clarity
(A) base image of picrosirius red-stained skin section.
(B) a-channel isolation after L*a*b conversion.
(C) combination of a-channel with positive region of b-channel.
(D) combined channels with contrast and brightness adjustment

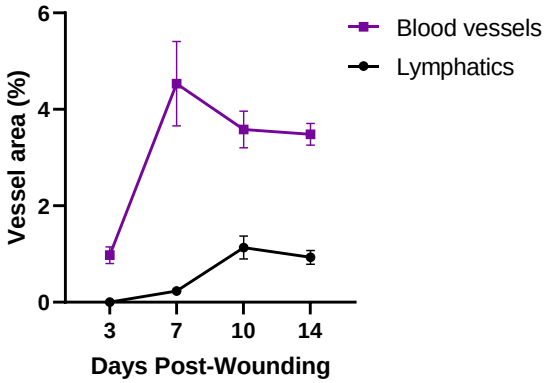

Figure S3 – Time course of wound angiogenesis and lymphangiogenesis
Quantification of CD31⁺ (blood vessel) area and Lyve-1⁺ (lymphatic vessel) area per hpf. Data are expressed as mean ± SEM. n=6 biological replicates and three independent experiments

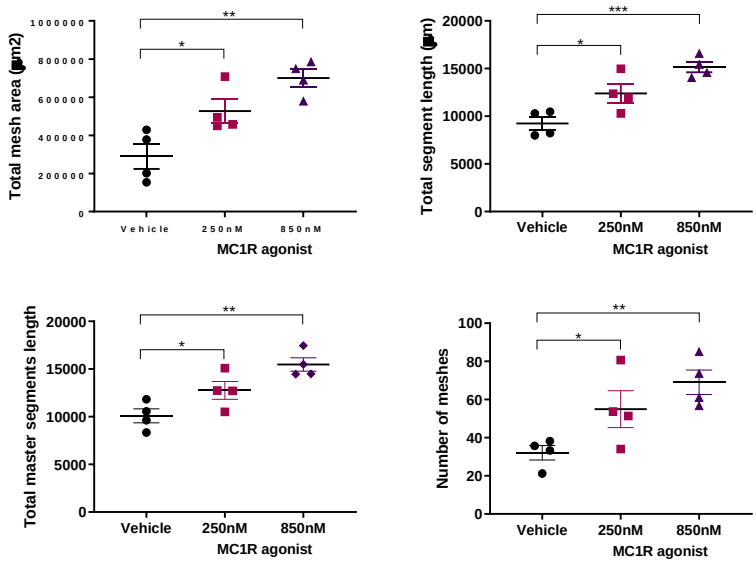

Figure S4 – MC1R agonist BMS-470539 promotes angiogenesis *in vitro*
Quantification of four key *in vitro* angiogenesis parameters in the presence and absence of MC1R agonist (250 nM and 850 nM). Data are expressed as mean ± SEM. Three independent experiments, each with five technical replicates.

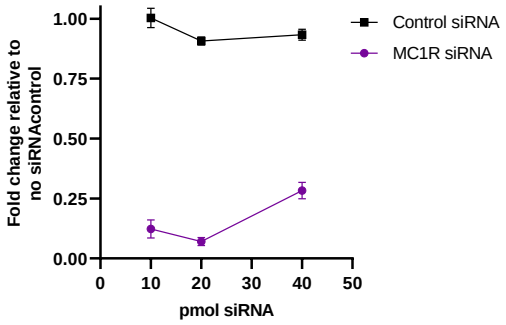

Figure S5 – MC1R siRNA knockdown vs control siRNA
Optimisation of MC1R siRNA knockdown. A dose of 20 pM was chosen. Data are expressed as mean ± SEM from three independent experiments, each with three technical replicates.

A

Ethical approval number

Animal number

dpi	Date	Wound		Wound Area				Activity and Movement	Behaviour			Irritation	Weight	Weight (%)	Pain	Bepanthen applied	Hair regrowth	Dressing		Photo Taken	Mash	Notes	Monitor (initials)	NVS spoken to	20% weight threshold	10% weight threshold
		Score	Exudate	Score	Size	Appearance		Score	Score	Scratching	Shaking							Appearance	Changes							
						Dead white tissue	Red ring around tissue																			
BASELINE	10.3.22												36								Yes				28.8	32.4
1	11.3.22	1	No Exudate	1	Growing larger	Yes	No	0	0	No	No	No	35.8	99.44%	0	No	No	Adherent	No		Yes					
2	12.3.22	1	Clear Exudate	1	No Change	Yes	Yes	0	0	No	No	No	34.2	95.00%	0	No	No	Adherent	No		Yes					
3	13.3.22	1	Clear Exudate	1	No Change	Yes	Yes	0	0	No	No	No	35.6	98.89%	0	No	No	Adherent	No		Yes	bit of crustiness next to dressing (leaked wound exudate)				
4	14.3.22	1	Clear Exudate	1	No Change	Yes	Yes	0	0	No	No	No	36.5	101.39%	0	No	No	Adherent	No		Yes	bit of crustiness next to dressing (leaked wound exudate)				
5	15.3.22	1	Clear Exudate	1	No Change	Yes	Yes	0	0	Yes	No	No	36.2	100.56%	0	No	No	Adherent	No		Yes	bit of crustiness next to dressing (leaked wound exudate)				
6	16.3.22	1	Clear Exudate	1	No Change	Yes	No	0	0	No	No	No	34.2	95.00%	0	No	No	Edges lifted	No		Yes					
7	17.3.22	1	Clear Exudate	1	No Change	Yes	No	0	0	No	No	No	34.2	95.00%	0	No	No	Adherent	Yes		Yes	Debrided, dressing change + PL treatment				
8	18.3.22	1	Clear Exudate	1	No Change			0	0	No	No	No	34.8	96.67%	0	No	No	Adherent	No		Yes					
9	19.3.22	1	Clear Exudate	1	No Change			0	0	Yes	No	No	34.3	95.28%	0	No	No	Adherent			Yes	bit of crustiness next to dressing (leaked wound exudate)				
10	20.3.22	1	Clear Exudate	1	No Change			0	0	No	No	No	34.2	95.00%	0	No	No	Adherent	Yes		Yes	Dressing change and PL treatment.				
11	21.3.22	1	Clear Exudate	1	No Change			0	0	No	No	No	33.7	93.61%	0	No	No	Adherent	No		Yes					
12	22.3.22	1	Clear Exudate	1	No Change			0	0	No	No	No	33.6	93.33%	0	No	No	Edges lifted	Yes		Yes	Large, sloughy, wet wound. Crusty. PL and dressing change.				
13	23.3.22	1	Clear Exudate	1	No Change			0	0	No	No	No	33.9	94.17%	0	No	No	Adherent	No		Yes	bit of crustiness next to dressing (leaked wound exudate)				
14	24.3.22	1	Clear Exudate	1	No Change			0	0	No	No	No	34	94.44%	0	No	No	Adherent	No		Yes					

B

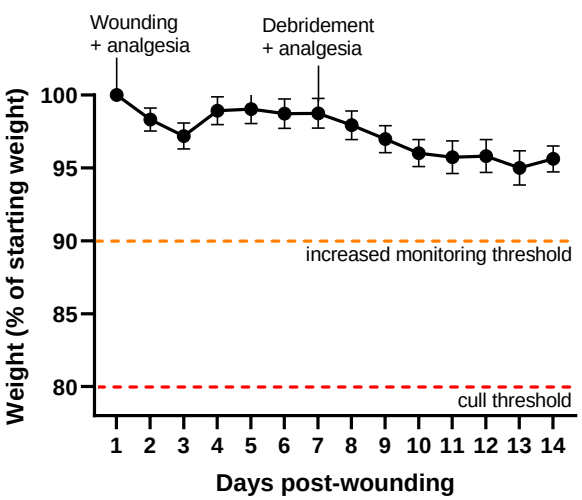

C

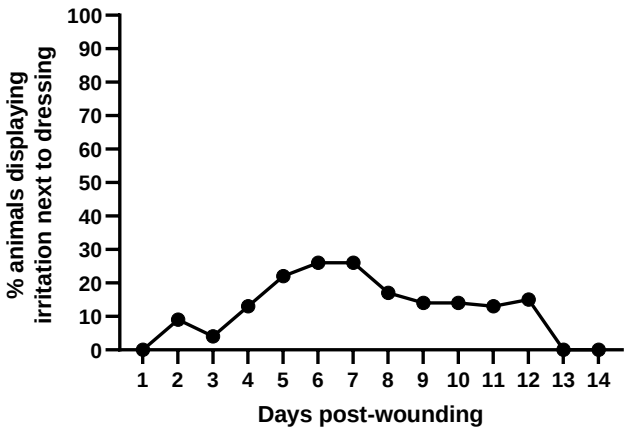

Figure S6 – Murine chronic wounds are very well tolerated

(A) Example monitoring record of wound features, animal behaviour and weight to ensure humane and ethical treatment.

(B) Minimal weight loss indicates that the chronic wound protocol is well tolerated by the aged mice. Data displayed as mean ± SEM (n=24).

(C) Up to 30% of mice displayed minor skin irritation next to the Tegaderm dressing. When this was observed Bepanthen cream was applied to soothe the area and prevent the irritation from worsening (n=24).

	Patient details				
Code	Sex	Age	Wound location	Duration of wound	Diagnosis
1D	F	77	Leg	2 years	Diabetic ulcer
2D	M	59	Ankle	7 years	Diabetic ulcer
4D	F	59	left hallux	4 years	Diabetic ulcer
5D	F	60	Left foot, 3rd toe	5 years	Diabetic ulcer
8D	M	60	right shin	1 year	Diabetic ulcer
9D	F	57	lateral anterio left leg	1 year	Diabetic ulcer
10D	F	73	left posterior heel	6 months	Diabetic ulcer
11D	F	59	top of right middle finger	2 weeks	Diabetic ulcer
14D	M	87	lateral border of left foot	3 months	Diabetic ulcer
4P	F	44	Buttock	6 months	Pressure ulcer
8P	F	73	right medial heel	8 months	Pressure ulcer
9P	F	78	right greater trochanter	not recorded	Pressure ulcer
12P	F	68	left ischium	not recorded	Pressure ulcer
13P	M	72	left ischium	7 months	Pressure ulcer
17P	F	52	left shoulder	2 months	Pressure ulcer
18P	M	12	sacral area	1 year	Pressure ulcer
6V	F	83	left ankle	6 months	Venous ulcer
7V	F	77	right mid anterior shin	1 year	Venous ulcer
8V	M	52	left medial malleolus	10 months	Venous ulcer
9V	M	89	left ankle	5 months	Venous ulcer
10V	M	62	left lower leg	6 weeks	Venous ulcer
11V	F	62	left medial malleolus	2 weeeks	Venous ulcer
13V	F	71	lateral aspect right foot	9 months	Venous ulcer
15V	F	77	left medial malleolus	6 months	Venous ulcer
16V	M	67	right leg	1 year	Venous ulcer
17V	M	69	back of lower right calf	3 years	Venous ulcer
18V	F	89	left shin	3 months	Venous ulcer
19V	M	67	lower left leg	1 year	Venous ulcer
20V	F	69	right medial malleolus	6 years	Venous ulcer
21V	M	94	left anterior fibula	4 months	Venous ulcer
22V	M	34	lateral left lower leg	6 months	Venous ulcer
28V	M	63	left ankle	1 year	Venous ulcer
31V	F	73	left ankle	2 years	Venous ulcer
32V	F	88	right posterior distal leg	unknown	Venous ulcer
33V	F	87	lower left leg	3 years	Venous ulcer
02_VL	M	59	anteromedial portion of left shin	1 year	Venous ulcer
04_VL	F	74	right lower leg	7 months	Venous ulcer
05_VL	M	80	right lateral malleolus	unknown	Venous ulcer
06_VL	F	82	gaiter region of left leg	3 years	Venous ulcer
07_VL	F	86	right medial malleolus	7 months	Venous ulcer
08_VL	F	71	left medial ankle	5 months	Venous ulcer
09_VL	M	92	right lower medial leg	8 weeks	Venous ulcer
10_VL	F	81	Left lower leg	2 months	Venous ulcer

Figure S7 – Donor information

	DFU (n = 9)	PU (n = 7)	VLU (n = 28)	mean
Fibrinous exudate	100%	100%	100%	100%
Hyperproliferative epidermis	89%	86%	100%	92%
Parakeratosis	67%	57%	78%	67%
Hypogranulosis	78%	100%	100%	93%
PMN infiltrate	89%	100%	100%	96%
NETs	44%	71%	78%	65%
Spongiosis	67%	86%	100%	84%
Hemosiderin	56%	0%	96%	51%
Extravasated erythrocytes	89%	71%	100%	87%
Vasculitis	89%	100%	100%	96%

Figure S8 – Prevalence of key histomorphological features of human chronic wounds according to wound category

	Mouse	Human
Fibrinous exudate	100%	100%
Hyperproliferative epidermis	100%	92%
Parakeratosis	75%	67%
Hypogranulosis	100%	93%
PMN infiltrate	100%	96%
NETs	60%	65%
Spongiosis	80%	84%
Hemosiderin	10%	51%
Extravasated erythrocytes	90%	87%
Vasculitis	100%	96%

Figure S9 – Comparison of the prevalence of key features of human chronic wounds in mouse and human
Key features were scored by two independent assessors for 10 preclinical mouse wounds and 44 human chronic wounds (average of DFU, VLU and PU in Fig. S8).

	Vehicle	MC1R agonist
Fibrinous exudate	100%	100%
Hyperproliferative epidermis	100%	100%
Parakeratosis	75%	33%
Hypogranulosis	100%	100%
PMN infiltrate	100%	100%
NETs	60%	33%
Spongiosis	80%	0%
Hemosiderin	10%	0%
Extravasated erythrocytes	90%	33%
Vasculitis	100%	67%
Fat necrosis	100%	100%

Figure S10 – Prevalence of key histomorphological features of human chronic wounds in vehicle-treated and MC1R agonist-treated murine chronic wounds

	C57Bl/6J	MC1Re/e
Fibrinous exudate	100%	100%
Hyperproliferative epidermis	100%	100%
Parakeratosis	75%	57%
Hypogranulosis	100%	100%
PMN infiltrate	100%	100%
NETs	60%	100%
Spongiosis	80%	100%
Hemosiderin	10%	57%
Extravasated erythrocytes	90%	0%
Vasculitis	100%	100%
Fat necrosis	100%	100%

Figure S11 – Prevalence of key histomorphological features of human chronic wounds in wildtype C57Bl/6J and MC1Re/e murine chronic wounds

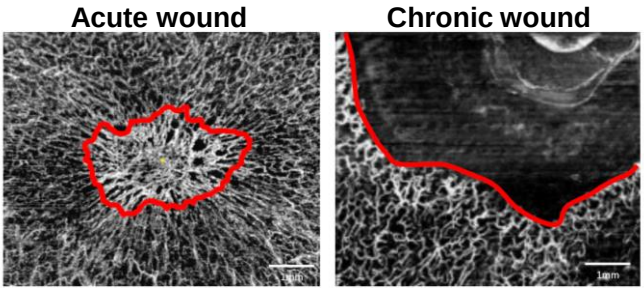

Figure S12 – OCT imaging of acute (A) and chronic (B) wounds at 7 dpi

(A) OCT enables visualisation of the perfused vasculature, demonstrating the increased vessel density in acute wounds during repair in comparison to the surrounding tissue (n=6).

(B) Human chronic wounds exhibit poor angiogenesis. Our preclinical wound model replicates this feature, displaying an almost complete lack of wound bed perfusion (n=2).

Wound margin is highlighted in red according to structural OCT imaging.

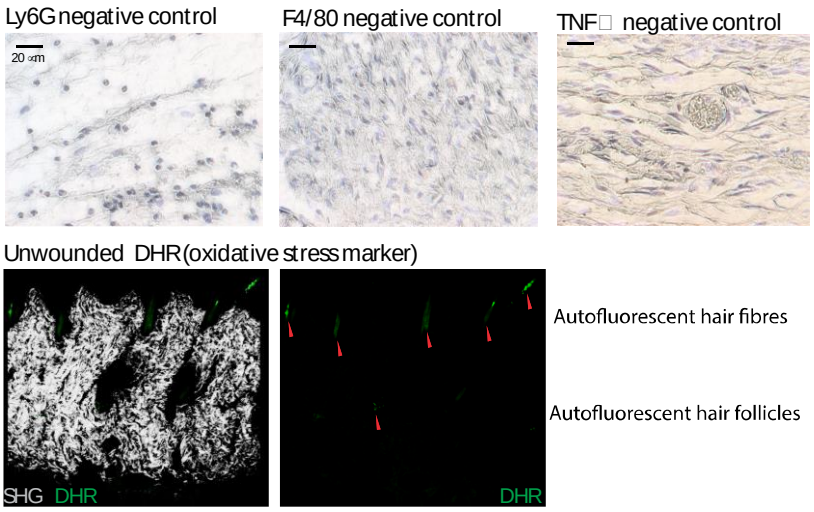

Figure S13 Negative controls

(A) Negative controls for immunohistochemical staining for Ly6G (neutrophils), F4/80 (macrophages) and TNFα.

(B) Negative controls for immunofluorescence staining of skin wound sections showing autofluorescent hair fibres and follicles.